

UNIVERSITY OF BIRMINGHAM

University of Birmingham
Research at Birmingham

Leader -cells coordinate Ca²⁺ dynamics across pancreatic islets in vivo

Salem, Victoria; Delgadillo Silva, Luis; Suba, Kinga; Georgiades, Eleni; Mousavy Gharavy, S. Neda; Akhtar, Nadeem; Martin-Alonso, Aldara; Gaboriau, David C. A.; Rothery, Stephen M.; Stylianides, Theodoros; Carrat, Gaelle; Pullen, Timothy J.; Pal Singh, Sumeet; Hodson, David; Leclerc, Isabelle; Shapiro, A. M. James; Marchetti, Piero; Briant, Linford J. B.; Distaso, Walter; Ninov, Nikolay

DOI:

[10.1038/s42255-019-0075-2](https://doi.org/10.1038/s42255-019-0075-2)

License:

Other (please specify with Rights Statement)

Document Version

Peer reviewed version

Citation for published version (Harvard):

Salem, V, Delgadillo Silva, L, Suba, K, Georgiades, E, Mousavy Gharavy, SN, Akhtar, N, Martin-Alonso, A, Gaboriau, DCA, Rothery, SM, Stylianides, T, Carrat, G, Pullen, TJ, Pal Singh, S, Hodson, D, Leclerc, I, Shapiro, AMJ, Marchetti, P, Briant, LJB, Distaso, W, Ninov, N & Rutter, GA 2019, 'Leader -cells coordinate Ca²⁺ dynamics across pancreatic islets in vivo', *Nature*, vol. 1, pp. 615-629. <https://doi.org/10.1038/s42255-019-0075-2>

[Link to publication on Research at Birmingham portal](#)

Publisher Rights Statement:

This is the accepted version of the following article: Salem, V, Delgadillo Silva, L, Suba, K, Georgiades, E, Mousavy Gharavy, SN, Akhtar, N, Martin-Alonso, A, Gaboriau, DCA, Rothery, SM, Stylianides, T, Carrat, G, Pullen, TJ, Pal Singh, S, Hodson, D, Leclerc, I, Shapiro, AMJ, Marchetti, P, Briant, LJB, Distaso, W, Ninov, N & Rutter, GA. (2019) 'Leader -cells coordinate Ca²⁺ dynamics across pancreatic islets in vivo', *Nature*, vol. 1, pp. 615-629, which has been published in final form at <https://doi.org/10.1038/s42255-019-0075-2>

General rights

Unless a licence is specified above, all rights (including copyright and moral rights) in this document are retained by the authors and/or the copyright holders. The express permission of the copyright holder must be obtained for any use of this material other than for purposes permitted by law.

- Users may freely distribute the URL that is used to identify this publication.
- Users may download and/or print one copy of the publication from the University of Birmingham research portal for the purpose of private study or non-commercial research.
- User may use extracts from the document in line with the concept of 'fair dealing' under the Copyright, Designs and Patents Act 1988 (?)
- Users may not further distribute the material nor use it for the purposes of commercial gain.

Where a licence is displayed above, please note the terms and conditions of the licence govern your use of this document.

When citing, please reference the published version.

Take down policy

While the University of Birmingham exercises care and attention in making items available there are rare occasions when an item has been uploaded in error or has been deemed to be commercially or otherwise sensitive.

If you believe that this is the case for this document, please contact UBIRA@lists.bham.ac.uk providing details and we will remove access to the work immediately and investigate.

1
2
3
4
5
6
7
8
9
10
11
12
13
14
15
16
17
18
19
20
21
22
23
24
25
26
27
28
29
30
31
32
33

Leader β cells coordinate Ca^{2+} dynamics across pancreatic islets
in vivo

Victoria Salem^{1,†}, Luis Delgadillo Silva^{2†}, Kinga Suba¹, Eleni Georgiadou¹, S. Neda Mousavy Gharavy¹, Nadeem Akhtar², Aldara Martin-Alonso¹, David C.A. Gaboriau⁴, Stephen M. Rothery⁴, Theodoros Stylianides³, Gaëlle Carrat¹, Timothy J. Pullen⁵, Sumeet Pal Singh², David J. Hodson^{6,7}, Isabelle Leclerc¹, A.M. James Shapiro⁸, Piero Marchetti⁹, Linford J.B. Briant¹⁰, Walter Distaso¹¹, Nikolay Ninov^{2,12*} and Guy A. Rutter^{1*}

¹Department of Medicine, Imperial College London, London, UK, ²DFG-Center for Regenerative Therapies, Technische Universität Dresden, Dresden, Germany, ³Loughborough University, Loughborough, UK, ⁴FILM, Imperial College London, London, UK, ⁵Department of Diabetes, Faculty of Life Science and Medicine, King's College London, London, UK, ⁶Institute of Metabolism and Systems Research (IMSR), University of Birmingham, Edgbaston, UK, ⁷Centre for Endocrinology, Diabetes and Metabolism, Birmingham Health Partners, Birmingham, UK; and COMPARE University of Birmingham and University of Nottingham Midlands, ⁸ Clinical Islet Laboratory and Clinical Islet Transplant Program, University of Alberta, Edmonton, Alberta, Canada, ⁹University of Pisa, Pisa, Italy, ¹⁰Radcliffe Department of Medicine, University of Oxford, Oxford, UK. ¹¹Imperial College London, UK, ¹²Paul Langerhans Institute Dresden of the Helmholtz Center Munich at the University Hospital Carl Gustav Carus of TU Dresden, German Center for Diabetes Research.

[†]Equal contributions

*Corresponding authors: g.rutter@imperial.ac.uk; v.salem@imperial.ac.uk; nikolay.ninov@tu-dresden.de

34 **ABSTRACT**

35

36 Pancreatic β cells form highly connected networks within isolated islets. Whether this
37 behaviour pertains *in vivo*, after innervation and during continuous perfusion with blood, is
38 unclear. Here, we use the recombinant Ca^{2+} sensor GCaMP6 to assess glucose-regulated
39 connectivity in living zebrafish *D. rerio*, and in murine or human islets transplanted into the
40 anterior eye chamber. In each setting, Ca^{2+} waves emanated from temporally-defined leader
41 β cells and 3D connectivity across the islet increased with glucose stimulation. Photo-
42 ablation of zebrafish leader cells disrupted pan-islet signalling, identifying these as likely
43 pacemakers. Correspondingly, in engrafted mouse islets, connectivity was sustained during
44 prolonged glucose exposure, and super-connected “hub” cells were identified. Granger
45 causality analysis revealed a controlling role for temporally-defined leaders, and
46 transcriptomic analyses a discrete hub cell fingerprint. We thus define a population of
47 regulatory β cells within coordinated islet networks *in vivo*. This population may drive Ca^{2+}
48 dynamics and pulsatile insulin secretion.

49

50 **WORDS: 150**

51

52 **Keywords:** Pancreatic islet, zebrafish, functional imaging, Ca^{2+} dynamics, GCaMP6, β cell,
53 *in vivo*, connectivity, photo-ablation, transcriptomics, cluster analysis, Granger causality.

54 **BACKGROUND.**

55

56 Defective insulin secretion underlies diabetes mellitus, a disease affecting almost 1 in 8 of
57 the adult population worldwide, consuming 10 % of healthcare budgets of westernized
58 societies (<https://www.idf.org/>). Impaired secretion is absolute in type 1 diabetes and relative
59 in type 2 diabetes ¹.

60

61 Individual β cells within the pancreatic islets possess all of the enzymatic machinery required
62 for glucose sensing and insulin secretion ^{2, 3}, although marked heterogeneity exists at the
63 transcriptomic ^{4, 5, 6, 7}, metabolic ⁸, electrophysiological ^{9, 10} and secretory ¹¹⁻¹³ levels.
64 Questions remain over whether this heterogeneity has any functional significance, and
65 could, for example, contribute to the pulsatile release of insulin ¹⁴.

66 Connections between individual β cells ^{15, 16} are essential for the normal control of hormone
67 secretion ^{10, 14, 17}. Using Ca^{2+} imaging of isolated islets *in vitro* two distinct, but
68 complementary, ways of analysing β cell connectivity have emerged. Earlier studies
69 described an increase in the number of correlated cell pairs using Pearson-based analysis,
70 which assesses similarities between the Ca^{2+} traces for individual cells over time ^{18, 19}. This
71 strategy revealed that stimulation with glucose or glucagon like peptide-1 causes pan-islet
72 increases in β cell connectivity which are disrupted under conditions mimicking type 2
73 diabetes (e.g. “gluco(lipo)toxicity”). More recently, we have applied an approach based on
74 signal binarization ²⁰ and reported that a subset of 5-8 % β cells form super-connected
75 “hubs” within the interconnected network ¹⁸. We also demonstrated that these cells are likely
76 to serve as pacemakers ²¹. Both of these approaches utilise the term “connectivity” to
77 describe the functional coactivity of β cells within an islet.

78 The behaviour of the isolated islet in culture ^{18, 21} is likely to differ significantly from that *in*
79 *vivo* where islets are continuously perfused with blood and receive complex neural inputs.
80 Imaging of the islet within the intact pancreas *in vivo* is, however, challenging and requires
81 exteriorisation of the whole organ. A powerful alternative approach is the engraftment of
82 islets into the anterior eye chamber ²². Combined with the use of stably-expressed,
83 recombinant fluorescent probes ^{23, 24} this creates an optically-accessible platform allowing
84 repeated measurements over time if required ²⁵. Here, we use this strategy, alongside an
85 analogous genetic modification of the zebrafish ²⁶ to record multilayer β cell Ca^{2+} dynamics
86 in the intact living animal ²⁷. Pancreatic islets display a largely conserved size, but partly
87 species-specific ²⁸ arrangement of neuroendocrine cell types ²⁹, important for the proper
88 control of insulin secretion ¹⁷. In the zebrafish, most of the pancreatic endocrine cells are
89 located in a single primary islet ²⁷. By 5 days post fertilization (dpf) (as used in these

90 experiments) zebrafish larvae have developed a primary islet which contains an average of
91 30 β cells that express mature markers like Ucn3l²⁶. Later in the juvenile stage, the
92 zebrafish still possesses the large, embryonically-derived primary islet and has also
93 developed many smaller secondary islets³⁰. We have previously shown that the primary
94 zebrafish islet responds *in vitro* to glucose²⁶ and ablation of β cells at this developmental
95 stage leads to glucose intolerance in the larva³¹. Thus, by 5 dpf the primary islet is glucose
96 responsive and systemically connected, serving as an excellent model to study islet β cell
97 coordination.

98

99 We demonstrate that glucose induces strongly co-ordinated pan-islet Ca^{2+} responses in
100 each setting, with a definable point of origin and propagation characteristics in three
101 dimensions. In zebrafish, the ablation of “leader” cells, i.e. those which respond first to
102 glucose challenge, results in a dampening of the response of the islet to subsequent
103 stimulation with glucose, redolent to the effects of optogenetic inactivation of “hub” cells in
104 the isolated mouse islet²¹. In the mouse, analyses based on signal binarization and Monte
105 Carlo-like shuffling/randomisation²¹ demonstrate the existence of a population of super-
106 connected cells under stimulatory conditions *in vivo*. Moreover, causality analysis^{32, 33} unites
107 these observations in fish and mouse by demonstrating that temporally-defined “leader cells”
108 are also those that were causally the most closely linked to other β cells, whilst analyses of
109 single cell RNASeq data suggests they may possess a unique transcriptional profile. Hence,
110 we demonstrate that a functional β cell hierarchy exists *in vivo*, and may control pulsatile
111 insulin secretion.

112

113

114 **METHODS**

115

116 *Zebrafish husbandry.*

117 Zebrafish wild type (WT) AB, WIK and TL were used in all the experiments. Zebrafish were
118 raised in standard conditions at 28 °C. Established transgenic lines used in this study were
119 *Tg(ins:gCaMP6s;cryaa:mCherry)*²⁶, *Tg(ins:cdt1-mCherry;cryaa:GFP)*³¹ and
120 *Tg(gata1a:DsRed)*²⁶. *Tg(ins:cdt1-mCherry)* was utilised in preference of a pan β cell marker
121 such as *Tg(ins:mKO-nls)* to allow for a clear separation of the spectra and simultaneous
122 signal recordings from the GCaMP and mCherry channels, which was particularly important
123 during fast imaging. All experiments were carried out in compliance with European Union
124 and German laws (Tierschutzgesetz) and with the approval of the TU Dresden and the
125 Landesdirektion Sachsen Ethics Committees (approval number: AZ 24D-9168,11-1/2013-14,
126 TV38/2015, T12/2016, and T13/2016, TVV50/2017, and TVV 45/2018)). All live imaging *in*
127 *vivo*, compound and glucose-injections, as well as experimental procedures were performed
128 with zebrafish larvae that did not exceed five days post fertilization (dpf), as stated in the
129 animal protection law (TierSchVersV §14). *Ex vivo* live-imaging of beta-cells was performed
130 with isolated islets from euthanized fish according to approval T12/2016.

131

132 *Zebrafish glucose measurements.*

133 Groups of ten larvae were pooled together, snap frozen in liquid nitrogen, and then stored at
134 -80°C. Following thawing on ice, 250 μ L of PBS were added and the larvae were sonicated
135 with an ultrasonic homogenizer (Bandelin, SONOPLUS), prior to centrifugation at 13,000g.
136 Glucose concentration was determined using the BioVision Glucose Assay Kit (Biovision Inc,
137 California, US) according to the manufacturer's instructions.

138

139 *Intra-cardiac injection in zebrafish.*

140 Injections were performed using pulled glass pipettes with a 5nL tip volume calibrated
141 microscopically (3.5" Drummond #3-000-203-G/X, Sutter pipette puller P-1000). A
142 pneumatic pico-pump (FemtoJet, Eppendorf), injecting pressure 500 hPa and compensation
143 pressure of 0 hPa, was used to deliver a 1 second injection into the pericardial cavity in the
144 agarose-mounted larva, assisted by a micromanipulator (InjectMan N2, Eppendorf). Doses
145 were 5 nL of 25 mM glucose and 5 nL insulin at 100 units/ml.

146

147 *Zebrafish live imaging.*

148 Embryos were treated with 0.003% (200 μ M) 1-phenyl 2-thiourea (PTU) to inhibit
149 pigmentation from 1 dpf onwards. At 4.5 dpf, the larvae were anaesthetized using 0.4g/L

150 Tricaine. The larvae were mounted in glass-bottomed microwell dishes (MatTek corporation)
151 using 1% low-melting agarose containing 0.4g/L Tricaine. After the agarose was solidified,
152 the dishes were filled with embryonic fish water and 0.4g/L Tricaine. Live imaging was
153 performed on an inverted laser scanning confocal system ZEISS LSM 780 inverted with a C-
154 Apochromat 40X/N.A. 1.2 water correction lens. In the *Tg(ins:GCaMP6s);Tg(ins:cdt1-*
155 *mCherry)* double-transgenic animals, we acquired the GCaMP6s and mCherry signals
156 simultaneously using the 488nm and 561nm laser lines. The GCaMP6s signal was rendered
157 in green and the nuclear signal in red. Videos were recorded at a 10 s/image (0.1 Hz) frame
158 rate unless indicated otherwise, with a Z-step thickness of 1.2 μm , covering on average 35
159 μm , and an XY resolution of 0.12 μm per pixel (512x512 pixels). Laser power was
160 maintained as low as possible (<1.5%) to minimise phototoxicity. For faster imaging, we
161 focused on a single plane, recording a frame every 300 milliseconds with an XY resolution of
162 0.08 μm per pixel (512x512 pixels).

163

164 *Zebrafish fast whole islet live imaging.*

165 Whole islet live-imaging at an acquisition rate of 0.8Hz, covering $\sim 700\mu\text{m}^3$, was achieved
166 using resonant scanner technology with an inverted laser scanning confocal system (Leica
167 SP5 MP) using an IRAPO L 25X/N.A. 0.95 water lens. Videos were recorded at ~ 0.8 Hz per
168 Z-stack ($\sim 700\mu\text{m}^3$), with a Z-step thickness of 4.5 μm , covering on average 70 μm in depth,
169 and an XY resolution of 0.24 μm per pixel (256x256 pixels). The resonant scanner was set
170 at 8,000 Hz with a bidirectional line scanning in order to achieve maximum speed.

171

172 *Selective two-photon laser ablation of leader cells.*

173 Live imaging and intra-cardiac glucose injections were performed as described above using
174 *Tg(ins:gCaMP6s;cryaa:mCherry)*, *Tg(ins:cdt1-mCherry;cryaa:GFP)* larvae. Images were
175 captured across a single confocal plane at an imaging acquisition rate of six frames/second
176 (6Hz). We performed three independent injections of glucose, separated by 5 min. intervals.
177 The “leader cell” (that is the temporally-defined first responder) was identified by eye based
178 on the changes in GCaMP6s-fluorescence after each glucose-injection. The larvae were
179 then transferred to a Leica SP5 MP confocal microscope, equipped with a two-photon laser
180 and 25X/0.95 N.A objective. A region of interest (ROI) was selected encompassing the
181 center of the nucleus of the cell to be ablated, covering a circle with an approximate
182 diameter of 0.5 μm . The cell of interest was then exposed to two-photon laser irradiation at
183 the output power of 2.0 W ($\lambda = 800$ nm) for 5 s to minimize possible damage to other areas.
184 We then performed live imaging and intra-cardiac injection again, using the protocol above,
185 and within 20 min. of irradiation, to record the response following cell ablation. Control cells

186 that were not the temporally-defined first responders (“followers”) were ablated with the
187 same methodology as leader cells. To ensure that the laser ablation technique was highly
188 localised to a single cell, as expected with this approach, we fixed islets immediately after
189 the laser cell-ablation (<10 min) then labelled them with insulin antibody and DAPI (see
190 below).

191 *Islet blood flow imaging in zebrafish.*

192 Imaging of islet blood flow was performed using triple transgenic larvae
193 *Tg(ins:GCaMP6s);Tg(ins:cdt1-mCherry);Tg(gata1a:DsRed)*. *Tg(gata1a:DsRed)* reporter
194 was used as a marker of red blood cells. Live imaging was performed on a ZEISS LSM 780
195 confocal microscope equipped with a C-Apochromat 40X/1.2 NA water correction lens. The
196 GCaMP6s and mCherry signals from β cells, and DsRed signals from blood cells, were
197 simultaneously acquired using the 488nm and 561nm laser lines. The GCaMP6s signal was
198 rendered in green. The blood cells and the nuclear signal of β cells were rendered in red.
199 We focused on a single plane and the videos were recorded at a frame rate of 1 frame/155
200 milliseconds (~6.4 Hz).

201 *Mechanical heart stop in zebrafish.*

202 To stop the blood flow in zebrafish larvae, a glass-pulled pipette (3.5” Drummond #3-000-
203 203-G/X, Sutter pipette puller P-1000), with a manually blunted end, was used to exert a
204 direct pressure into the heart. The heart was blocked for around 400 s. The mechanical
205 heart stopping was executed during live Ca^{2+} imaging in the *Tg(ins:GCaMP6s);Tg(ins:cdt1-*
206 *mCherry)* double-transgenic larvae, as described above. Videos were recorded at a 10 s
207 frame rate (0.1 Hz), and a Z-step thickness of 2.8 μm , covering on average 50 μm , with a
208 frame size of 512 x 512 pixels.

209 *Identification of dorsal- and ventral-bud derived β cells.*

210 The primary zebrafish islet contains both dorsal bud-derived β cells (DBC) and ventral bud-
211 derived β cells (VBC). To interrogate whether embryonic derivation affected the identity of
212 leader cells, we performed injection of mRNA encoding H2B-RFP to distinguish between D-
213 and VBCs based on label dilution³⁴. In this assay, DBCs retain the H2B-RFP label whereas
214 VBCs dilute it. We injected one-cell stage embryos with mRNA expressing H2B-mCherry.
215 We maxi-prepped the pCS2+H2B-mCherry plasmid, digested it with KpnI and in vitro
216 transcribed it using the SP6 Transcription Kit (Ambion, AM1340) to generate mRNA. We
217 injected 100pg of H2B-mCherry mRNA in each embryo. Larvae were mounted as described
218 above for whole islet live imaging and glucose-injections.

219 *Post mortem staining for cell ablation in zebrafish.*

220 After the live imaging was performed, and the leader cells were temporally identified, the
221 larvae were immediately fixed in 4% PFA overnight. Then the samples were permeabilized
222 with 1% PBT (Triton-X-100) for 1hr. To avoid non-specific primary antibody binding, we
223 blocked for 2hrs in PBTB (PBT + 4% BSA). Nuclear staining was performed using DAPI at
224 1:1000 dilution. After the immunostaining with anti-insulin (polyclonal guinea pig anti-Insulin,
225 Dako A0564, 1:300 dilution), the samples were mounted in Vectashield. The anti-insulin
226 antibody has been previously validated to mark β -cells in zebrafish by us using transgenic
227 lines that express GFP under the insulin promoter and was also recently validated to show
228 negative immunoreactivity in β -cells in homozygous mutant fish for the *insulina* gene (PMID:
229 30520733), confirming its high specificity. Images were acquired using Z-Stacks on a LSM-
230 780 Zeiss confocal microscope. For image analysis, the nuclei of the β cells were
231 segmented using the DAPI channel.

232

233 *Ex vivo imaging of primary and secondary zebrafish islets.*

234 The islet culture and imaging were performed as previously described³⁵. Primary and
235 secondary islets were isolated from three month post fertilization (mpf) *Tg(ins:gCaMP6s;*
236 *cryaa:mCherry)* animals. The islets were stimulated with a ramp of 10 and 20 mM D-glucose
237 (Sigma, G8270). The imaging culminated with the addition of 30mM KCl (Sigma, P9451) in
238 the same plate. Videos were recorded at a 2.5 s/image (0.25 Hz frame rate), in a single Z-
239 plane and with an XY resolution of 0.59 μ m per pixel (1024x1024 pixels). After imaging,
240 individual β cell ROIs were manually drawn using Image J. Fluorescence intensity (FI) was
241 normalized using the minimum and maximum values of FI across frames for each cell. Cells
242 which did not show an increase in GCaMP signal after KCl addition, were not included in the
243 analysis.

244

245 *Image analysis from in vivo imaging of zebrafish.*

246

247 The cumulative population response of β cells was quantified from maximum intensity
248 projections (MIP) of the z-stack. In the MIP, the islet area was delimited manually using the
249 Region of Interest (ROI) Manager in ImageJ (<https://imagej.net/Fiji>)³⁶. Using the ROI, the
250 integrated fluorescence intensity of GCaMP6s was extracted. The integrated fluorescence
251 intensity was normalized for the whole imaging time using the following formula:

252

253 $(F_T - F_{MIN}) / (F_{MAX} - F_{MIN}),$

254

255 where F_T is the integrated fluorescence intensity at a given time while F_{MAX} and the F_{MIN} are
256 the maximum and minimum values recorded during the live imaging session, respectively.

257

258 Single-cell signal analysis of GCaMP signal was performed either from single-confocal slices
259 covering a majority of imaged β cells (2D) or by segmenting the nuclei from the Z-stacks
260 using the nuclear mCherry signal (3D). For nuclear segmentation, we utilized the 3D image
261 suite in Image J, and the 3D iterative thresholding plugin³⁷. The following parameters were
262 set based on the estimated approximate nuclear size of β cells: minimum volume = 100
263 pixels; maximum volume = 1200 pixels; criteria method = “volume”; threshold method =
264 “volume”; value method = 10 units. This generated a voxel covering the nuclei of β cells.
265 Using the 3D ROI manager plugin, we extracted the integrated fluorescence intensity from
266 each voxel over time (FT). In order to create 3D plots, we first extracted the centroids from
267 each voxel and then plotted them using the R software and the package “rgl”. Single-cell
268 heat-maps based on 2D analysis were created using Excel and conditional formatting setting
269 the colors in a gradient from 0 to 1. For visualization, the brightness and contrast was
270 adjusted uniformly across the times series using ImageJ, and the tool Brightness/Contrast.

271

272 *Quantification of GCaMP6s fluorescence intensity in zebrafish images.*

273 For the quantification of changes in GCaMP6 fluorescence upon glucose or insulin injection
274 in Figure 1 and Supplementary Figure 1, the cumulative response of all imaged β -cells to
275 glucose injection was quantified. To this end, we compared the area under the curve based
276 on the normalized integrated fluorescence intensity 10 frames before and after the injections
277 of glucose or insulin (covering 200 seconds of imaging) using the formula:

278

$$279 (F_T - F_{MIN}) / (F_{MAX} - F_{MIN}),$$

280

281 For the quantification of changes in GCaMP6 fluorescence upon laser-cell ablation (Figure
282 4), the cumulative response of all imaged β cells to glucose injection was quantified. In this
283 case, the maximum value (F_{MAX}) was not used for normalization since such normalization
284 could mask the effect of loss of response following cell ablation due to normalization to
285 background fluorescence. Instead, we only subtracted the background from the imaging
286 session using the following formula:

287

$$288 (F_T - F_{MIN}) / F_{MIN}$$

289

290 The larvae were injected with three separate pulses of glucose before and after the ablation.
291 For each injection the GCaMP area under the curve was calculated covering 200 frames

292 after the glucose injection. The average area under the curve was calculated before and
293 after the ablation and plotted as \log_2 .

294

295 *Spatial drift correction OF ZEBRAFISH images.*

296 The red channel (cdt1-mCherry) signal from the β cell nuclei was used to correct for spatial
297 drift in the green GCaMP6s channel. A maximum projection of each Z-stack in the time
298 series was entered into the FIJI plugin “Descriptor-based series registration (2d/3d + t)”
299 ([https://imagej.net/Descriptor-based_registration_\(2d/3d\)](https://imagej.net/Descriptor-based_registration_(2d/3d)))³⁸, applying the model “Rigid (2d)”,
300 with “3-dimensional quadratic fit”. A sigma of 13 and threshold of 0.03 was applied to the
301 detection of nuclear signal, with a minimum number of three neighbors, redundancy of 1 and
302 a random sample consensus (Ransac) error of 5. Matching across time series was achieved
303 using global optimization, unless indicated otherwise. Stabilization in the Z dimension was
304 achieved using the Fiji “Reslice” command. The “Descriptor-based series registration (2d/3d
305 + t)” plugin was used with nuclei detection sigma set to 5 and with a threshold of 0.03.

306

307

308 *Mouse husbandry.*

309 Male C57Bl/6 wild type (WT) (18-25g) mice were purchased from Charles River, UK, and
310 used as donor islet recipients. For *in vivo* measurements of cytosolic Ca^{2+} in pancreatic β
311 cells, we generated mice that express GCaMP6f in β cells using the Cre-Lox system. Briefly,
312 we crossed Ins1Cre mice (provided by J Ferrer, this Department)^{39, 40} with mice that express
313 GCaMP6f downstream of a LoxP-flanked STOP cassette (The Jackson Laboratory, stock
314 no. 028865). Islets donated from either sex were used for transplantation. Mice were
315 housed in groups of six in individually-ventilated cages under controlled conditions (21-23°C;
316 12 h light: 12 h dark cycle). Male BALBc *nu/nu* (The Jackson Laboratory, stock no. 002019)
317 recipients were used for human islet transplantation. Animals had *ad libitum* access to
318 standard chow and water (irradiated for the immunocompetent mice). All animal procedures
319 were approved and performed under the UK Home Office Animals (Scientific Procedures)
320 Act 1986 (Project License to I.L., PA03F7F07 at Imperial College London. The project
321 licence received internal institutional ethical approval as well as external Home Office
322 approval).

323 *Generation of adenovirus expressing GCaMP6m (AV-GCaMP6m).*

324 A plasmid driving the expression of *GCaMP6m* under the control of the cytomegalovirus
325 (CMV) promoter (CMV-AVGCaMP6m) was generated using the pAdEasy system⁴¹. Briefly,
326 pGP-CMV-GCaMP6m plasmid (Addgene plasmid # 40754) was digested using *Bgl*II and

327 *Notl.* The released GCaMP6m fragment was then purified and ligated into pShuttle-CMV
328 vector (Addgene plasmid # 16403). CMV-GCaMP6m was inserted by recombination into the
329 adenoviral pAdEasy-1 vector (Addgene plasmid # 16400), and transformed into
330 electrocompetent BJ5183 cells. The isolated plasmid was subsequently amplified in reduced
331 recombination rate (recA1) NEB-10 β competent *E. coli* (New England BioLabs). Following
332 the transfection of AD293 cells with the linearized pAdEasy-CMV-GCaMP6m construct, cells
333 were harvested and lysed to release virions. The virus was further amplified and purified by
334 centrifugation on a CsCl gradient. Titration was performed by infecting AD293 cells with
335 serially diluted viral stocks, counting positive cells through GCaMP6m fluorescence.

336 *Islet transplantation into murine anterior chamber of the eye (ACE).*

337 Pancreatic islets were isolated and cultured as described previously ⁴². For transplantation,
338 10-20 islets were aspirated with a 27-gauge blunt eye cannula (BeaverVisitec, UK)
339 connected to a 100ul Hamilton syringe (Hamilton) via 0.4-mm polyethylene tubing (Portex
340 Limited). Prior to surgery, mice were anaesthetised with 2-4% isoflurane (Zoetis) and placed
341 in a stereotactic frame to stabilise the head. The cornea was incised near the junction with
342 the sclera, being careful not to damage the iris. Then, the blunt cannula, pre-loaded with
343 islets, was inserted into the ACE and islets were expelled (average injection volume 20 μ l for
344 10 islets). Carprofen (Bayer, UK) and eye ointment were administered post-surgery.

345 *In vivo Ca²⁺ imaging of AV-GCaMP6m infected murine islets in the ACE.*

346 Prior to transplantation into the ACE of recipients, isolated islets (from WT C57/BL6 donors,
347 <24 weeks old or human islet donations) were infected with AV-GCaMP6m *in vitro* at a
348 multiplicity of infection (MOI) of 20 for 24 h. This approach, which was expected to allow the
349 identification, if present, of functional islet sub-compartments (i.e. local groups of interacting
350 β cells) provided preferential infection of superficial β cells (1-2 cells deep). Of these, ~ 50 %
351 were infected. A minimum of four weeks was allowed for full implantation of transplanted
352 islets before imaging. Imaging sessions were performed with the mouse held in a
353 stereotactic frame and the eye gently retracted, with the animal maintained under 2-4%
354 isoflurane anaesthesia. All imaging experiments were conducted using a spinning disk
355 confocal microscope (Nikon Eclipse Ti, Crest spinning disk, 20x water dipping 1.0 NA
356 objective). The signal from AV-GCaMP6m fluorophore (ex. 488 nm, em. 525 \pm 25 nm) was
357 monitored in time-series experiments for up to 20 min. at a rate of 1 frame/sec. Ca²⁺ traces
358 were recorded for three min. prior to intraperitoneal (IP) glucose injection, with a mean blood
359 glucose reading (across five islets in five separate animals) of 8 mmol/L. Three minutes into
360 acquisitions mice received 150 μ l 30% (1.5g/kg) bolus of glucose intra-peritoneally (IP).
361 Blood glucose was subsequently measured on a glucometer (Accu-Chek, UK) at two-minute

362 intervals from a tail vein nick until the end of experiments. Injection of glucose at 180 s
363 raised blood glucose to an average of 28 mM for the remainder of the 10 min. imaging
364 series. Since the mouse imaging experiments are the first of their kind, sample size ($n=5$
365 islets in $n=5$ animals) was determined to be adequate based on the magnitude and
366 consistency of measurable differences between groups. This was in line with other studies
367 examining islets in the ACE ²².

368

369 *In vivo Ca²⁺ imaging of Ins1Cre-GCaMP6f islets in the ACE.*

370 Ins1Cre-GCaMP6f (ex.: 488nm, em. 525±25 nm) -expressing islets were isolated and
371 transplanted into WT recipients ($n=5$ islets in $n=5$ different animals), and imaged as
372 described above. Stream acquisitions of a single x/y plane of β cells recorded 2 min.
373 datasets at 3Hz. Islets ($n=5$ islets in $n=5$ different animals) were continuously monitored and
374 the focus was manually adjusted to counteract movement. Islets (in the same imaging
375 session) were imaged under both “low glucose” (2–6 mM) and “high glucose” (17-25 mM)
376 conditions (randomly ordered). Blood glucose (tail nick, Accu-chek glucometer) was
377 assessed at 2 min. intervals throughout. Low glucose readings were obtained following the
378 intravenous (IV) administration of insulin (Actrapid, 0.3ml of 1.0 iu/ml), and high glucose was
379 achieved with a 200 μ l 30% (2g/kg) IP bolus of sugar. At the end of experiments animals
380 were allowed to recover and were further monitored for an hour for potential post-operative
381 latent hypoglycaemia.

382 To extend the image acquisitions to collect 3-dimensional data (ie. three separate planes of
383 β cells across an islet), a piezo device was attached to the inverted objective. This allowed
384 for rapid, precise, 15 μ m z-movements such that a 3-slice z-stack could be obtained at a
385 whole-islet imaging rate of 1 fps. At this imaging speed, we were able to obtain 3D
386 connectivity readouts for low and high glucose conditions (as described above, $n=3$ islets in
387 $n=3$ different animals). As we became more expert with the ability of our platform, this
388 number of experiments was sufficiently powered to demonstrate the rise in connectivity from
389 low to high glucose in the 3D imaging experiments,

390

391 Finally, we examined islet Ca²⁺ dynamics during a longer period of glucose stimulation, to
392 exclude the possibility that pan-islet connectivity is related to spatially aggregated β cells
393 simply responding acutely and synchronously to a rise in circulating glucose concentration.
394 Five animals (five separate islets studied, in line with former acute experiments) were placed
395 under isoflurane anaesthesia for 60 minutes. At the start of the imaging session an IP
396 bolus of sugar was administered. This led to a slow and sustained rise in circulating blood

397 sugar (measured every 3-5 minutes via tail vein sampling, as before). 30-50 minutes into
398 this imaging session, a 10-minute single plane islet recording was taken at 1fps, manually
399 readjusted in real time for movement. This was performed at “high” glucose levels (i.e. when
400 blood sugar levels had risen after IP glucose injection to a high, steady level >12 mmol/L).
401 We also report connectivity at a previous stage in the imaging session (10-20 minutes in)
402 when circulating glucose levels were at an intermediate (medium glucose, 7-10 mmol/L)
403 range (but the islets were still exhibiting coordinated wave activity). In the same imaging
404 session, the islets were recorded following IV administration of insulin when circulating levels
405 of glucose were low (< 4 mmol/L). The same islet plane and β cell ROIs were investigated
406 under each of the three (low, medium and high) circulating glucose conditions. To ensure
407 that the findings from this experiment were unaltered with the use of another anaesthetic, we
408 repeated these experiments using ketamine (Zoetis) and xylazine (Bayer) (90 mg/kg and 4.5
409 mg/kg cocktail respectively), with similar findings.

410 *In vivo Ca²⁺ imaging of AV-GCaMP6m infected human islets*

411 We studied the behaviour of 11 individual human islets (four individual donors, age range
412 14-74 years, non-diabetic, BMI range 21.5 to 29.2; see Supplementary Figure 5) that had
413 been transduced with AV-GCaMP6m and transplanted into the ACE of
414 (immunocompromised) BALB/c *nu/nu* mice. A human donor with diabetes (female, 54 years
415 old, BMI 24.4, type 2 diabetic for 10 years, insulin dependent for the last 1.5 yrs) provided
416 islets for two experiments (separate islets in separate BALB/c *nu/nu* recipients). Human
417 islets were obtained from multiple institutions (co-authors AMJS at the University of Alberta,
418 Edmonton, Canada and PM at the University of Pisa, Italy). Permission for the use of
419 human tissue was provided at Imperial College by the Charing Cross Research Ethics
420 Committee, REC reference number 07/H0711/114. Human islets were obtained post
421 mortem with next of kin and local and ethical permission at the sites of procurement. There
422 was no selection procedure for the implantation of human donor islets, and they were
423 implanted into recipient mice as they became available. Donor data are fully anonymised
424 and no clinical data beyond age, gender, and cause of death were available.

425 Following an imaging protocol described for the *Ins1Cre-GCaMP6f* mouse studies above, we
426 measured human islet behaviour under imposed low (< 4 mM) and high (>7 mM) glucose
427 conditions. Since BALB/c mice are resistant to glucose rises under anaesthesia, there are
428 more successful imaging results in the low glucose state reported. *Image analysis.* Using
429 FIJI (Image J) software (see above), images in the time series were individually time
430 stamped, to maintain their absolute time information, before excluding frames where
431 resolution was poor or blurred by movement. Image series were then cropped and manually

432 aligned across all frames using a pre-defined region of interest (ROI) as reference. Creating
433 ROIs for analysis was guided by the emitted GCaMP fluorescence and the negative shadow
434 of nuclei. For the virally infected islets each ROI extended over the entirety of a cell, whereas
435 ROIs in experiments with transgenic islets covered sub-cellular regions in close proximity to
436 nuclei. Mean fluorescence intensity and XY(Z) co-ordinates for each cell within an islet
437 (ROIs) were compiled and processed for connectivity analysis.

438 *Pearson (R)-based connectivity analyses.*

439 Correlation analyses between the Ca^{2+} signal time series for all cell pairs in an imaged islet
440 were performed in MATLAB using a custom-made script (available upon request). Data
441 were smoothed using a retrospective averaging method (previous 10 values) and all traces
442 were normalised to F0. Two-sided averaging techniques were not applied as this would
443 have invalidated subsequent causality analyses. The correlation function R between all
444 possible (smoothed) cell pair combinations (excluding the autocorrelation) was assessed
445 using Pearson's correlation. Data are displayed as heatmap matrices, indicating individual
446 cell pair connections on each axes (min. = -1; max. = 1). Given that data were not normally
447 distributed (and hence resorting to either asymptotic p-values or Monte Carlo based ones
448 would not be useful), the data were subsequently subjected to a bootstrap resampling to
449 increase the accuracy of the confidence interval of the R statistic, and $p < 0.001$ was deemed
450 a statistically significant cell-cell connection. The Cartesian co-ordinates of the imaged cells
451 were then taken into account in the construction of connectivity line maps. Cell pairs ($R > 0.25$
452 AND $p < 0.001$ post bootstrap) were connected with a straight line, the colour of which
453 represented the correlation strength and was assigned to a colour-coded light-dark ramp
454 ($R = 0.25-0.5$ [green], $R = 0.5-0.75$ [yellow], $R = 0.75-1.0$ [red]). An average coefficient of
455 positive connectivity was computed for each condition, by averaging the positive R values
456 (excluding the auto-correlated cells) and the percentage of cells that were significantly
457 connected to one another was elicited, for the purposes of group comparisons.

458 We have not examined the immediate upstroke of an acute IV bolus of glucose i.e. from a
459 low to a high glucose setting. Consequently the "first responders" in the mouse datasets
460 refer to the first β cells observed to fire in a train of calcium waves during a period of more
461 prolonged elevated glucose.

462 *Signal binarization and Monte Carlo analysis.*

463 To investigate what happens in the tail of the distribution, and go beyond the analysis of
464 linear association provided by the Pearson correlation coefficient, we also looked at
465 association between activity regimes. This analysis was performed as described previously

466 ^{20, 21}. In brief, cells were considered to be either “on” or “off” if the fluorescent signal
467 exceeded a 20% noise threshold above baseline. Binarized data for each cell pair were
468 assessed for co-synchronicity using the co-activity statistic $C_{ij} = T_{ij}/(\sqrt{[T_i \cdot T_j]})$ where C is a co-
469 activity coefficient (0 to +1), T_i and T_j represent the time spent in the active state for each
470 given cell and T_{ij} represents the time during which both cells are active. Pairs were
471 considered linked if their statistic displayed a higher than chance ($p < 0.01$) probability of
472 interaction *versus* a Monte Carlo permuted version of the binarized matrix dataset. A
473 probability distribution function of these connections (pooled across five islets) was
474 presented as a log-log plot to look for a power law relationship, the strength of which was
475 quantified by the coefficient of determination (R^2)³⁸.

476 *Granger analysis.*

477 The mouse *Ins1Cre* GCaMP6f-expressing islet series were subjected to a Granger Causality
478 analysis^{32, 33}. Individual cell-cell pairs were separately analysed (time lag 1-3 secs, $p < 0.001$)
479 with a Bonferroni multiple comparison test. Granger-defined leaders, i.e. those cells with the
480 greatest number of causally-linked followers, were compared with the temporally-defined
481 leaders whose firing (in the high glucose condition) preceded the remainder of the β cell
482 population. Granger leaders that persisted when the low, medium and high glucose
483 experiments were performed on the same network of β cells were spatially located on the
484 islet map to understand their spatial distribution.

485

486 *Zebrafish transcriptomic analysis (single cell RNAseq).*

487 For single-cell RNA-Seq of the zebrafish pancreatic cells using the 10x Genomics platform,
488 cell suspension was prepared from primary islets of six 2 mpf *Tg(ins:BB1.0L)*²⁶ using the
489 protocol described in⁴³ ($n=6$ animals). The cell suspension was passed over a 30 μ m cell
490 filter (Miltenyi Biotec, 130-041-407) to remove debris and cell-aggregates, adjusted with
491 HBSS (without Ca, Mg) to a density of 800 cells/ μ l, and diluted with nuclease free water
492 according to the manufacturer’s instructions to yield 5000 cells. Subsequently, the cells were
493 carefully mixed with reverse transcription mix before loading the cells on the 10X Genomics
494 Chromium system⁴⁴. After the gel emulsion bead suspension underwent the reverse
495 transcription reaction, emulsion was broken and DNA purified using Silane beads. The cDNA
496 was amplified with 10 cycles, following the guidelines of the 10x Genomics user manual. The
497 10X Genomics single cell RNA-seq library preparation – involving fragmentation, dA-Tailing,
498 adapter ligation and indexing PCR – was performed based on the manufacturer’s protocol.
499 After quantification, the libraries were sequenced on an Illumina NextSeq 550 machine using

500 a HighOutput flowcell in paired-end mode (R1: 26 cycles; I1: 8 cycles; R2: 57 cycles), thus
501 generating ~45 mio fragments. The raw sequencing data was then processed with the
502 'count' command of the Cell Ranger software (v2.1.0) provided by 10X Genomics with the
503 option '--expect-cells' set to 5000 (all other options were used as per default). This yielded
504 2625 cells. To build the reference for Cell Ranger, zebrafish genome (GRCz10) as well as
505 gene annotation (Ensembl 87) were downloaded from Ensembl and the annotation was
506 filtered with the 'mkgtf' command of Cell Ranger (options: '--
507 attribute=gene_biotype:protein_coding --attribute=gene_biotype:lincRNA --
508 attribute=gene_biotype:antisense'). Genome sequence and filtered annotation were then
509 used as input to the 'mkref' command of Cell Ranger to build the appropriate Cellranger
510 Reference. Data are deposited at the GEO repository with an accession number
511 GSE123662.

512

513 *Cluster analysis.*

514 scRNA-Seq data from C57BL/6 mouse islets were downloaded from NCBI GEO
515 (GSE84133)⁴⁵. UMI-filtered counts were analysed using the Seurat package⁴⁶. The data
516 were filtered and normalised then highly variable genes identified for PCA analysis and
517 graph-based clustering. In the mouse data, insulin, glucagon and somatostatin cells were
518 largely separated into distinct clusters. The initial clustering of the fish data produced a
519 single cluster containing cells expressing *ins*, *gcga* and *sst1.1* (listed by ENSEMBL as the
520 zebrafish orthologue of the H. sapiens SST gene; similar data were obtained using the
521 *sst1.2* gene). This 'endocrine' cluster was separated from the other cells and re-clustered,
522 producing distinct clusters for these three genes. The *ins*+ clusters were combined and the
523 few remaining cells positive for *gcga*, *sst1.1* or *gip*, or negative for *ins*, were excluded. Within
524 this group of β cells, the intersection between the upper quartile of *gck* expression and lower
525 quartile of *ins* expression was identified as putative hub cells, based on the properties of
526 these cells described previously²¹. Genes differentially expressed between the putative hub
527 cells and remaining β cells were identified using Wilcoxon rank sum test and the upregulated
528 genes thus identified were tested for statistical overrepresentation of Gene Ontology (GO)
529 BP terms using Pantherdb.org⁴⁷. Insulin-positive mouse cells were analysed in a similar
530 manner except that putative hub cells were classified as the intersection between the upper
531 quartile of *Gck* expression and the lower two quartiles of *Ins1* expression.

532

533 *Statistical analysis.*

534 Statistical significance between two conditions was assessed using paired or unpaired
535 Student's t-test. Interactions between multiple conditions were determined using one- or two-
536 way ANOVA (with Tukey's or Bonferroni posthoc tests). Analyses were performed using
537 Graph Pad Prism (GraphPad Software version 8.0) and MATLAB (Mathworks) and
538 significant p-values are described in each relevant section. Values are plotted as mean \pm
539 SEM, unless otherwise stated.

540 *Data availability*

541 The data that support the findings of this study and the Matlab codes for the various
542 connectivity analyses described above are available from the corresponding authors upon
543 request. Data repositories for the transcriptomic analyses are referenced in the appropriate
544 sections. The Reporting Summary for this manuscript, which details experimental design,
545 statistical analyses and reagents is available as a separate document. No datasets were
546 excluded from the mouse experiments and in all cases (except for the human diabetic islet
547 experiments, as described) the connectivity results between low and high glucose states
548 were in the same direction.

549

550

551

552

553

554 **RESULTS**

555 ***Glucose controls β cell connectivity in the living zebrafish.***

556 To explore Ca^{2+} dynamics *in vivo* with single-cell resolution we first imaged at low acquisition
557 speeds (0.1 Hz; Supplementary Figure 1a) zebrafish larvae (4-5dpf) expressing GCaMP6s
558 under the insulin promoter (Figure 1a) and the nuclear β -cell marker *Tg(ins:cdt1-mCherry)*,
559 which marks $86 \pm 6.6\%$ ($n=5$ islets) of all β -cells at 5 dpf. We focused our study on the
560 primary zebrafish islet, which is the only islet present at this stage. We first used *ex vivo*
561 imaging to directly compare the glucose-responsiveness of the primary and secondary islets
562 dissected from adult fish³⁵. As expected, β cells from the primary and secondary islets
563 showed apparent Ca^{2+} influx upon stimulation with 10 and 20 mM glucose or depolarization
564 with potassium chloride (KCl; $n=3$ primary and $n=3$ secondary islets) (Supplementary Movie
565 1). Thus, the primary islet is an adequate system for studying the glucose-stimulated Ca^{2+}
566 dynamics in zebrafish β cells, as well as representing the major site of insulin storage.

567

568 *In vivo* imaging of GCaMP6s-expressing β cells in larvae revealed the existence of
569 endogenous oscillations in cytosolic free Ca^{2+} (12/12 animals studied; Supplementary Figure
570 1 a-c, Supplementary Movie 2). This activity was inhibited by intracardiac injection of insulin,
571 which lowered whole-animal glucose (Supplementary Figure 1, c-f, Supplementary Movie 3),
572 indicating that the oscillatory Ca^{2+} signal was due to elevated circulating levels of glucose
573 that are measurable by 4-5 dpf⁴⁸. Ca^{2+} dynamics were also decreased after a transient
574 suppression of blood flow by a temporally controlled heart block (Supplementary Movie 4).
575 Time-lapse imaging of red-blood cells and β cells confirmed that the zebrafish islet is
576 perfused in larvae (Supplementary Movie 5). Taken together, these results reveal
577 endogenous β cell Ca^{2+} oscillations likely to be involved in the systemic sensing of glucose
578 *in vivo* in the zebrafish.

579

580 We next explored the impact of increasing the levels of glucose in the zebrafish circulation.
581 We performed intra-cardiac injection of glucose, allowing for rapid entry of the sugar into the
582 circulation (Figure 1b-d). After a short lag (20-50 s) this manoeuvre led to a rapid increase in
583 cytosolic Ca^{2+} concentrations (assessed as the time take to achieve a GCaMP6 signal >20%
584 above baseline) in β cells across the islet (Figure 2 b-d; Supplementary Movie 6), and
585 corresponded to the time-dependent increases in whole animal glucose concentrations
586 assessed separately (Figure 1e).

587

588 We next sought to determine the degree to which the β cell population in these experiments
589 was connected before and after stimulation with glucose, firstly at low imaging speeds of

590 0.1Hz (Figure 2 and Supplementary Figure 2) then at high imaging speeds of 3 Hz (Figure
591 3a-d). We derived Pearson-based functional connectivity maps (see Methods) of pairwise
592 comparisons between the Ca^{2+} traces of individual cells^{21, 49}. At low imaging speeds, 10-
593 15% of cells hosted a connection to another cell prior to glucose injection, and this rose
594 significantly to ~50 % after glucose injection ($p<0.001$, Figure 2 c-f). A similar, dramatic
595 increase ($p<0.01$) was seen for connection strength (i.e. Pearson's correlation, R; Figure
596 2e). Of note, the temporally-defined "leader" cells (first responders to glucose stimulation)
597 were amongst the most highly connected. For example, in the animal shown in Figure 2,
598 Ca^{2+} increases were first observed in two out of nine cells (cell 2 and cell 6; Figure 2b), and
599 these cells were the most connected on Pearson analysis at high glucose (connected to
600 seven or eight other cells out of a total of nine analysed; Supplementary Table 1).

601

602 Recorded at a higher acquisition rate (3 Hz) across a single plane, β cells again displayed
603 modest connectivity at low glucose (pre-injection ~20%; Figure 3d). The increases in
604 intracellular Ca^{2+} which followed glucose injection (Figure 3a and b) were associated with a
605 significant rise in correlation coefficient (Figure 3c) as well as a marked increase in the
606 number of functionally-connected cell pairs (post-injection ~88%, $p<0.0001$, Figure 3d).
607 Approached with a Pearson analysis at high glucose, essentially every cell became strongly
608 connected to every other cell. Finally, whole islet live-imaging at an acquisition rate of
609 0.8Hz, covering ~700 μm^3 was achieved. In this way, it was possible to resolve the majority
610 (20) cells within the primary islet of the zebrafish (Figure 3e) and extract their signal spatially
611 in three dimensions (Figure 3f; Supplementary Movie 7). We then undertook 3D connectivity
612 analysis on three separate zebrafish islets before and after glucose stimulation (as before).
613 Figure 3g shows the 3-dimensional connectivity analysis for one fish islet with mean
614 coefficient of correlation rising from 40.1 to 89.1 and fraction of connected cells rising from
615 11.2 to 92.3 % with a glucose bolus. Results for the other two islets showed the same rise in
616 Pearson coefficient (83.2 to 91.7 and 44.9 to 85.1) and rise in connected cells (33.3 to
617 55.5% and 16.7 to 38.1%). We therefore conclude that functional connectivity occurs across
618 the entire fish islet and that 2-dimensional (single plane) connectivity analysis in the fish
619 accurately reflects what occurs across the entire islet.

620

621 ***Ablation of leader cells prevents subsequent Ca^{2+} waves in the zebrafish embryo.***

622

623 In order to determine whether "leader" (first responder) cells may serve a regulatory role, as
624 demonstrated previously for mouse islets *in vitro*²¹, we used cell ablation through two
625 photon laser irradiation (Figure 4, Supplementary Movies 8 and 9). Animals were challenged
626 with three separate pulses of intracardiac glucose introduced before and after irradiation of

627 either leader or follower cells ($n=20$ leader and $n=20$ follower cell ablation experiments).
628 Whereas ablation of follower cells had no discernible effect on the subsequent Ca^{2+} spikes,
629 ablation of leader cells led to a significant reduction in the total islet GCaMP response
630 (Figure 4). Only targeted cells revealed evidence of nuclear destruction, while the
631 neighbouring cells showed no obvious damage (Supplementary Figure 4). Moreover, we
632 show that islet blood flow remains unaltered following the ablation of the cells using bright-
633 field imaging before and after the ablation (Supplementary Movies 8 and 9). Thus, the
634 targeted ablation of a single β cell in vivo does not appear to perturb either local endothelial
635 cells or the rest of the β cells in the islet.

636

637 ***Leader cells do not preferentially derive from the dorsal or ventral buds in the***
638 ***zebrafish embryo.***

639

640 The primary zebrafish islet contains both dorsal bud-derived β cells (DBC) and ventral bud-
641 derived β cells (VBC). To interrogate whether embryonic derivation affected the identity of
642 leader cells, we performed injection of mRNA encoding H2B-RFP to distinguish between D-
643 and VBCs based on label dilution³⁴. In this assay, DBCs retain the H2B-RFP label whereas
644 VBCs dilute it. We performed 4D live Ca^{2+} imaging and glucose injections in these embryos.
645 In the three islets examined, two revealed label-retaining cells as leaders, meanwhile one
646 islet revealed a leader cell that was H2B-negative. Supplementary Movie 10 shows a 3D
647 reconstruction of one representative experiment in which the leader cell was H2B-RFP-
648 positive. This implies that both the D- and VBCs can become leader cells. It is important to
649 note that, in these experiments, we did not observe impaired responsiveness of DBCs to
650 glucose stimulation *per se*, indicating that DBCs indeed exhibit characteristics of functional β
651 cells.

652

653 ***Glucose enhances Ca^{2+} dynamics and elicits increases in β cell- β cell connectivity in***
654 ***islets in the living mouse.***

655

656 We next extended our analysis to islets from the adult mouse, with superficial β cell layers
657 infected with adenoviral GCaMP6m, before engraftment into the anterior chamber of a
658 recipient mouse eye (ACE)²². Non- β cells are not infected by this protocol due to the
659 absence of the cognate receptor (Coxsackie virus receptor⁵⁰). Using animals maintained
660 under general anaesthetic, we collected data at acquisition speeds of 1 Hz, before and after
661 IP glucose injection (see Methods).

662

663 Ca^{2+} dynamics were increased in response to a rise in circulating glucose. The proportion of
664 significantly Pearson-connected cells increased on average from $38 \pm 11\%$ to $65 \pm 9\%$ ($n=5$
665 islets in 5 animals, $p=0.028$) with a non-significant ($p=0.11$) rise in the mean coefficient of
666 connectivity from $0.54 \pm 0.03\%$ to $0.63 \pm 0.04\%$.

667

668 We subsequently generated islets from transgenic mice expressing GCaMP6f highly
669 selectively in the β cell, under the control of *Cre* recombinase expressed from the *Ins1* locus
670 ^{39, 40}, and transplanted into the mouse ACE as above. Almost every β cell ($\sim 95\%$) ²¹ within
671 the transgenic islet expressed the Ca^{2+} probe, allowing us to interrogate the activity of many
672 more cells per islet, including those localised more deeply in the islet core (typically 50 to
673 100). We captured data at higher rates (up to 3 Hz) under low and high circulating glucose
674 conditions (see Methods).

675

676 Strikingly, and in contrast to islets infected with adenoviral GCaMP6f, we observed wave-like
677 behaviour of the β cell Ca^{2+} increases in all islets (examined separately and in ten different
678 animals) at high circulating glucose levels (Supplementary Movies 11, 12 and 13, Figure 5b
679 and 6c). Ca^{2+} waves were initiated at discrete sites (Supplementary Movie 12), with
680 propagation velocities of $12.0 \pm 3.4 \mu\text{m/s}$ ($n=5$ wave bursts). As shown in the example in
681 Figure 5B and Supplementary Movie 13, whilst most cells were quiescent under low glucose
682 conditions, high circulating glucose levels was associated with runs of highly-coordinated
683 oscillations, even after prolonged glucose exposure (10 minutes, Figure 5b and Figure 6a).

684

685 We were able to quantify connectivity using both Pearson and binarized data approaches
686 (Figures 5 and 6). As observed in the fish, high circulating glucose was associated with a
687 significantly higher mean coefficient of connectivity, and proportion of connected cells,
688 versus the low glucose condition, as revealed by Pearson analysis (Figures 5 c-e and
689 Supplementary Figure 5a). We also used a piezo device to allow for fast acquisition of β cell
690 readouts in three separate cell layers under low and high circulating glucose conditions, to
691 investigate whether β cell connectivity existed in 3-dimensions (see Methods). Of note, this
692 significant rise in pan-islet β cell connectivity at high circulating glucose levels also occurred
693 between cells that were more than a layer apart on 3D imaging (Figure 5c-e and
694 Supplementary Figure 5a). The Pearson analysis was, however, unable to detect significant
695 differences in co-activities required for identification of super-connected cells/hubs. In
696 contrast, application of a binarized approach (see Methods) ²¹ revealed scale free network
697 topography in which $8.7 \pm 3.7\%$ of cells hosted the majority (60-100%) of connections
698 (Figures 6 a-b and Supplementary Figure 6). Pooled over all five islets examined, the R^2
699 value for this power law distribution was 0.62.

700

701 Finally, we examined islet Ca^{2+} dynamics over 10 minutes at steady state high glucose
702 levels (and also acquired medium and low glucose acquisitions from the same cells in the
703 same 1 h-long imaging study), to exclude the possibility that pan-islet connectivity is related
704 to spatially aggregated β cells simply responding acutely and synchronously to a rise in
705 circulating glucose concentration. Blood sugar readings recorded over these imaging
706 sessions did not reveal oscillating glucose levels, excluding the trivial possibility that glucose
707 oscillations themselves are driving Ca^{2+} oscillations (Figure 5b). A concerted, elevated
708 Pearson correlation and percentage β cell connectivity was achieved over these longer
709 acquisitions with higher (and sustained) circulating glucose levels (Figure 6a).

710

711 ***Prospective analysis (Granger causality)***

712

713 Given the challenges of a direct interventional strategy such as photo-ablation in the mouse
714 eye, we deployed an alternative, mathematical approach to examine the potential role of
715 leader cells as pacemakers. Granger analysis³² provides a means of assessing whether a
716 given time series may be useful in forecasting another, i.e. is predictive of a causal
717 relationship. This supported our visual identification of first responding (leader) cells. As
718 shown in Figure 6 c-e, we observed that those four cells (“leaders”, Figure 6C; this islet is
719 shown in Supplementary Movie 11), which fired first during a prolonged run of Ca^{2+} pulses,
720 were always represented as leaders in the second and third bursts but not always in fourth
721 and fifth bursts (if present). However, leader cells identified temporally as among the first five
722 responding cells under high glucose conditions were invariably the most highly connected on
723 independent Granger analysis (Supplementary Table 2). Granger analysis of the top 10
724 most highly connected cells during the prolonged imaging sessions (10 minute acquisitions
725 at high, medium and low glucose, of the same cross section of islet/same β cell ROIs)
726 revealed one cell to be a Granger leader in all three states and, interestingly, to be in the
727 same region (neighbouring) 2-5 other Granger leaders in the medium and high state – which
728 was also the segment of islet from which waves emanated (data not shown).

729

730 Interestingly, this analysis provided no evidence that peri-capillary cells were more likely to
731 be “Granger leaders” (average distance from leader cells to the nearest capillary: 2.2 ± 1.9
732 μm versus $2.3 \pm 1.8 \mu\text{m}$ for follower cells, $n=25$, $p>0.05$). Hence, differences between cells in
733 the arrival time for glucose from the blood stream are unlikely to be the determining factor for
734 initiating Ca^{2+} waves.

735

736 ***Engrafted human islets are highly connected.***

737

738 To corroborate our findings in a further species we studied the behaviour of 11 human islets
739 transduced with AV-GCaMP6m and transplanted into the ACE of (immunocompromised)
740 BALB/c *nu/nu* mice (see Methods) We observed a non-significant rise in human islet
741 coefficient of correlation from 0.39 to 0.59, and a corresponding rise in β cell connectivity
742 from 56% to 76% between low and high circulating glucose conditions (Supplementary
743 Figure 5b). Intriguingly, in the two islets that came from a donor with longstanding Type 2
744 Diabetes (see Methods), the switch from low to high circulating blood sugar was associated
745 with an unexpected drop in Pearson R (53 to 24 and 44 to 32), and an equivalent fall in the
746 proportion of connected β cells (from 30% to 20% and 29% to 27%; Supplementary Figure
747 5c). This observation opens up the possibility that the loss of insulin secretory function that
748 occurs in Type 2 diabetes is linked to abnormal connectivity patterns.

749

750 ***Transcriptomic analysis.***

751

752 To determine whether hub/leader cells may possess a discrete molecular signature *versus*
753 followers we analysed RNASeq data from fish and mouse β cells. We have previously
754 reported ²¹ that hub cells in the mouse islet are characterised by relatively high levels of
755 glucokinase (Gck) immunoreactivity, and lower levels of Insulin, Pdx1, Nkx6,1 staining.

756

757 We first generated and analysed a zebrafish transcriptomic data set (10x Genomics) and
758 were able to identify a cluster of mainly endocrine cells expressing *sst1.1*, *gcga* or *ins*.
759 Further clustering of these 'endocrine' cells produced clusters of likely delta (*sst1.1*), alpha
760 (*gcga*) and β (*ins*) cells (Supplementary Figure 6a-b). Putative hub cells were identified
761 based on the higher glucokinase and lower insulin expression previously observed in mouse
762 islets. The intersection of the upper quartile of *gck* expression and the lower quartile of *ins*
763 expression identified 9 % of β cells as putative hub cells (Supplementary Figure 6c).
764 Enrichment and gene ontology (GO) analysis revealed elevated expression of genes in
765 hub/leaders associated with mitochondrial metabolism (oxidative phosphorylation and
766 respiratory electron transport chain) and generation of precursor metabolites and energy,
767 among other terms (Supplementary Figure 6 d-e). Interestingly, the re-clustering of the
768 'endocrine' cluster resulted in two distinct and approximately equally-sized β cell
769 populations. The putative hub cells identified here came almost entirely from a single cluster,
770 suggesting these may represent one end of a continuous distribution within this cluster
771 rather than a distinct subset.

772

773 Similar analysis of mouse islet data revealed that the intersection of the upper quartile of
774 *Gck* and lower two quartiles of *Ins1* expression contained 11 % of β cells (Supplementary
775 Figure 6 f-h). Genes upregulated in this cluster were overrepresented in the GO terms
776 “Glycolysis” and “Generation of precursor metabolites and energy” (Supplementary Figure 6
777 i-j), potentially indicating that these are more metabolically active cells, as observed above in
778 the zebrafish case.

779

780

781

782

783 **DISCUSSION**

784

785 The principal aim of the present study was to explore β cell coordination in the islet *in vivo* in
786 the living animal. Here, we have studied the zebrafish islet in its natural state and the mouse
787 islet under conditions of vascularisation and innervation which closely recapitulate those of
788 the islet within the pancreas⁵¹⁻⁵³. We show that, despite the quite profound differences
789 between the isolated and *in vivo* islet, coordinated β cell responses to glucose stimulation
790 display many of the features previously described *in vitro*, including the emergence of cells
791 which may govern islet-wide Ca^{2+} dynamics and hence pulsatile insulin secretion.

792

793 **Islet-wide Ca^{2+} dynamics in the living zebrafish**

794

795 We demonstrate firstly that, in the zebrafish, increases in blood glucose lead to a
796 coordinated increase in β cell cytosolic Ca^{2+} across the islet. Using Pearson R analysis, we
797 describe a well-connected network of β cells in the zebrafish islet that responded in a
798 coordinated fashion to glucose stimulation. These findings align well with those of Markovic
799 *et al*⁴⁹ in murine pancreatic slices, and our own findings in isolated mouse islets¹⁸. Given
800 the small size of the zebrafish islet at this developmental stage, it was not possible to apply
801 scale-free network theory to these datasets. However, we were able, using a direct
802 interventional approach akin to the use of optogenetics in isolated murine islets^{21, 54}, to
803 demonstrate that those cells which were the first to exhibit a Ca^{2+} increase (“leaders”) may
804 perform a role as regulators of the activity of other β cells. Photo-ablation of leader, but not
805 follower cells, resulted in a significant abrogation of Ca^{2+} dynamics in remaining β cells in
806 terms of their time to response as well as their overall calcium response to a glucose
807 challenge. We also provided evidence to establish that this methodology produced no
808 collateral damage, i.e. did not affect cells other than the single β cell that was targeted. We
809 would emphasize that this approach offers significant advantages over the use of
810 optogenetics for β cell targeting, notably the fact that further genetic modification required to
811 express an optogene (e.g. a photoswitchable channel or pump- shown to influence β cell
812 activity)^{21, 54, 55} is avoided, and axial resolution is high. Photo-ablation of leader, but not
813 follower cells, resulted in the abrogation of Ca^{2+} dynamics (Fig. 4c), pointing to a role for the
814 former as regulators of β cell activity across the islet.

815

816 It was particularly interesting to note the findings of the *ex vivo* imaging studies that directly
817 compared *in vitro* glucose-responsiveness of the primary and secondary zebrafish islets.
818 The only discernible difference we observed between the primary and the much later-
819 forming secondary islets *ex vivo* pertained to a faster Ca^{2+} response of the latter, which was

820 evident at 10 mM glucose. This faster response is likely to reflect the much smaller size of
821 the secondary islets and, hence, the easier penetration to the islet core of glucose when
822 added *ex vivo*. It is important to note also that we have not observed impaired
823 responsiveness to glucose stimulation of β cells originating from the dorsal pancreatic buds
824 *in vivo*, consistent with our recent findings that DBCs are functional²⁶. Finally, when imaged
825 in culture, the zebrafish islets exhibit seemingly uncoupled behaviours, revealing the
826 glucose-sensitivity of individual β -cells^{26,56}. In contrast, β -cells show synchronized
827 responses to glucose *in vivo* (this study and⁵⁶). Thus, the unperturbed conditions of the *in*
828 *vivo* environment might be critical for the coupling of β -cells.

829

830

831 **Islet-wide Ca^{2+} dynamics in the engrafted mouse islet**

832

833 In mammalian islets, we routinely observed clear trans-islet, glucose-induced Ca^{2+} waves
834 (10/10 Ins1Cre-GCaMP6-expressing islets examined in independent experiments), whereas
835 these are not always observed in Fluo8-loaded isolated islets *in vitro*²¹. This may reflect the
836 presence of nerves and blood vessels in our *in vivo* model as well as, conceivably, the better
837 preservation of β cell identity, gap junctions, etc.². Moreover, the use of transgenic islets, in
838 which the genetically-encoded Ca^{2+} sensor is present in almost the entire (~95%) β cell
839 population after recombination using the Ins1Cre transgene^{21, 39, 40}, is likely to facilitate the
840 detection of waves. Thus, we were able to image cells located some distance away from the
841 islet periphery, with adequate resolution to 4-5 cell depths in the z-plane (Supplementary
842 Movie 14). Furthermore, with a rapid piezo device we were able to demonstrate that Ca^{2+}
843 dynamics were strongly coordinated across β cells that were separated by another layer of
844 cells. However, the present studies do not address the question of how connections
845 across the islet are established (e.g. roles for islet inter-neurons, paracrine factors, etc.).
846 Other interventional approaches (e.g. using multiphoton, light sheet or other imaging
847 techniques) will be necessary to explore these phenomena in the future.

848

849

850 By imaging large numbers of cells simultaneously, and subjecting the resulting datasets to
851 binarization analysis, we revealed the existence of scale free networks, as previously
852 described *in vitro*²¹. This set of experiments examined the nature of islet behaviour *in vivo*
853 through two different but complementary lenses. Pearson R analysis highlights the pan-islet
854 β cell connectivity (both in terms of the number of connected cells and their strength of
855 correlation) in response to elevated circulating glucose levels. Separately, we have
856 demonstrated using data binarization and shuffling²¹ that these cells are connected in a way

857 that fits with the presence of super-connected hubs. Recently, Rupnik and colleagues⁵⁷
858 have reported, using mouse islets located within pancreatic slices, that at adequate
859 acquisition speeds (10Hz), Pearson analysis can reveal a connectivity probability distribution
860 function that obeys a power law, at least initially following glucose stimulation.

861

862 To corroborate our zebrafish findings, where disruption of the temporally-defined “leader”
863 cells abrogated subsequent islet-wide Ca^{2+} responses to glucose, we performed
864 independent mathematical causality analysis of all the β cells that were recorded in the
865 mouse islet. Selecting a causality time lag consistent with that observed between the first
866 responders and the rest of the β cells (i.e. 1 s)³², we revealed that these were indeed the
867 most highly causally linked to the activity of all other cells in the islet. Both the experimentally
868 established zebrafish “leaders” and the mathematically causally-identified mouse “leaders”
869 are reminiscent of previously identified *in vitro* hub cells²¹, insofar as both regulate Ca^{2+}
870 dynamics observed in the rest of the islet being imaged. Our present findings also indicate
871 that temporal and spatial dynamics need to be considered in identifying likely regulatory
872 populations. For example, essentially normal blood flow is maintained in the engrafted islet.
873 One may have predicted, therefore, that “leader” β cells would be those located immediately
874 adjacent to blood vessels. In contrast, we observed no greater likelihood of cells in this
875 domain of the islet initiating waves than for cells more remotely located. We also observed
876 that islets retained a baseline Ca^{2+} activity (and indeed a degree of connectedness between
877 β cells) even in the low glucose state. Thus, at low circulating glucose levels Ca^{2+} waves
878 were occasionally observed above noise levels with the same amplitude and frequency of
879 bursts as at high glucose, but less commonly. Within a single train of waves, the starting
880 point was often, but not always conserved, and was frequently seen at the islet rim. Such
881 waves often propagated circumferentially, although there were some that appeared to move
882 towards the islet core. Taken together, this hints that functional networks already exist at low
883 glucose concentrations, under conditions in which the majority of cells are not yet firing.
884 These pre-activated networks may then expand and work as a coordinating unit to drive the
885 recruitment of followers.

886

887 It was also important to demonstrate a retention of the high connectivity readouts in islets
888 that had been exposed to prolonged elevated glucose levels. Many previous studies on
889 isolated islets and β cells reveal heterogeneous Ca^{2+} responses to glucose stimulation⁵⁸.
890 Indeed, we are not aware of existing literature supporting the notion that β cells have an
891 identifiable (and identical) resting Ca^{2+} oscillation signature. Nevertheless, it was important
892 here to exclude the possibility that the high connectivity observed at high glucose levels is a

893 phenomenon related to spatially aggregated (i.e. intra-islet) β cells simply responding
894 acutely and synchronously to a rise in circulating glucose concentration. The high
895 connectivity findings in islets that had been imaged for an hour at elevated circulating
896 glucose levels serve to argue against the possibility that connectivity is an acute
897 phenomenon of this type since, in an uncoordinated system, over a 60 min. imaging
898 protocol, with glucose levels that are not rapidly varying, one would expect de-synchrony to
899 emerge. Finally, the first responders (and Granger leaders) are defined during Ca^{2+} pulses
900 at essentially constant glucose (although glucose may drift gradually over multiple Ca^{2+}
901 waves during these recordings).

902 Several questions remain with respect to the Ca^{2+} waves identified here: to what extent are
903 their starting points spatially defined relative to nerves and other islet cell types? How do
904 they propagate? Are they always associated with pulses of insulin secretion? Further studies
905 are also required to determine whether “leader” cells are functionally essential to islet health,
906 are pre-fated or can assume leader characteristics over time that relate to altered islet
907 function under metabolic stress or in diabetes.

908

909 **Towards the molecular identity of hub/leader cells**

910

911 Prior to the current study, our understanding of the differences in molecular identity between
912 hub and follower cells was fragmentary²¹. To explore this question here in an unbiased,
913 transcriptome-wide manner, we have leveraged the known properties of mouse hub cells,
914 i.e. elevated expression (at the protein level) of *Gck* and relatively weak expression of
915 *Insulin*. We note that confirmation of similar properties for the fish hub/follower populations
916 (i.e. high *Gck*low *insulin*low *Pdx1*-immunoreactivity) was not possible here due to the
917 absence of suitable antibodies for the *D. rerio* *Gck* protein. Nonetheless, if we assume
918 similar properties for the fish and mouse hub cells our analyses reveal that, in both species,
919 a population exists with characteristics which may be expected of these cells, notably
920 elevated expression of genes involved in glucose metabolism and, in zebrafish, of genes
921 involved in mitochondrial metabolism. Of note, a similar β cell population was identified
922 recently in the mouse by Pospisilik and colleagues⁵⁹. Future studies, involving the direct
923 isolation of hubs and followers based on function (e.g. Ca^{2+} dynamics), are needed to
924 confirm or refute these findings.

925

926 **Summary**

927

928 In conclusion, we show here that examined in the living animal β cells within the islet are
929 highly connected in three dimensions and that this connectivity is tightened in response to a
930 glucose challenge. As predicted from previous studies of isolated islets *in vitro*^{18, 21}, we
931 show that critical subpopulations of β cells, which appear to generate Ca^{2+} waves, serve a
932 regulatory role in the zebrafish and appear likely to do so in the mammalian islet as well. At
933 this stage, it is not possible to investigate whether the leader cells are a distinct population
934 with a distinct origin and development. However, we provide a preliminary analysis, using an
935 imputation approach based on previously-described proteomic properties of these
936 populations²¹, to suggest they possess a distinct transcriptomic signature. Future
937 challenges will involve isolating and characterising these cells, as well as assessing the
938 stability of each sub group (i.e. leader/hubs and followers). Taken together, our data provide
939 further evidence for a division of labour within the islet *in vivo* in three different species,
940 reinforcing the importance of β cell heterogeneity for normal glucose-responsiveness.

941

942 **Acknowledgements.**

943

944 VS was supported by a Diabetes UK Harry Keen Clinician Scientist 15/0005317. G.A.R. was
945 supported by a Wellcome Trust Senior Investigator Award (WT098424AIA), MRC
946 Programme grants (MR/R022259/1, MR/J0003042/1, MR/L020149/1) and Experimental
947 Challenge Grant (DIVA, MR/L02036X/1), MRC (MR/N00275X/1), Diabetes UK
948 (BDA/11/0004210, BDA/15/0005275, BDA 16/0005485) and Imperial Confidence in Concept
949 (ICiC) grants, and a Royal Society Wolfson Research Merit Award. I.L. was supported by
950 Diabetes UK Project Grant 16/0005485 and D.J.H. by a Diabetes UK R.D. Lawrence
951 (12/0004431) Fellowship, a Wellcome Trust Institutional Support Award, and MRC
952 (MR/N00275X/1) and Diabetes UK (17/0005681) Project Grants. N.N. received funding from
953 the DFG–Center for Regenerative Therapies Dresden, Cluster of Excellence at TU Dresden
954 and the German Center for Diabetes Research (DZD), as well as research grants from the
955 German Research Foundation (DFG), the European Foundation for the Study of Diabetes
956 (EFSD) and the DZD. L.J.B.B. was supported by a Sir Henry Wellcome Postdoctoral
957 Fellowship (Wellcome Trust, 201325/Z/16/Z) and a Junior Research Fellowship from Trinity
958 College, Oxford. This project has received funding from the European Research Council
959 (ERC) under the European Union’s Horizon 2020 research and innovation programme
960 (Starting Grant 715884 to D.J.H.) and from the Innovative Medicines Initiative 2 Joint
961 Undertaking under grant agreement No 115881 (RHAPSODY) to G.A.R. and P.M. This Joint
962 Undertaking receives support from the European Union’s Horizon 2020 research and
963 innovation programme and EFPIA. We would like to thank Professor Per-Olof Berggren
964 (Karolinska Institute, Sweden and Imperial College London), Alejandro Caicedo and Raynor

965 Rodriguez (University of Miami), and Drs Pauline Chabosseau, Marie-Sophie Nguyen-Tu
966 and Bryn Owen (Imperial College London), for valuable advice and support with surgery and
967 imaging. With thank Rebecca Callingham (Imperial College) for assistance with human islet
968 culture.

969

970

971 **Author Contributions**

972 VS, NN and GAR designed the study, LDS and NA performed the zebrafish experiments,
973 VS, KS, AMA, and IL undertook the mouse studies, GC and KS performed virus
974 preparations, DCAG, SMR, KS and VS developed movement correction macros, EG,
975 SNMG, NA, TS, DJH and LB contributed to connectivity analysis, DJH and LB provided code
976 for connectivity analysis, VS and WD developed connectivity and Granger scripts and
977 undertook all connectivity analyses, PM and AMJS provided human islets and KS and VS
978 undertook studies on these preparations. TJP, NA and SPS performed transcriptomic and
979 bioinformatics analyses. GAR, VS, LDS and NN wrote the manuscript with contributions from
980 all authors.

981

982 G.A.R. has received grant funding from Servier and is a consultant for Sun Pharma. All
983 others authors declare no competing financial interests

984

985

986

987

Reference List

988

989

990

991

1. DeFronzo,R.A., Ferrannini,E., Zimmet,P., & Alberti,G. International Textbook of Diabetes Mellitus 4 th Edition. 2015. Hoboken, New Jersey, Wiley-Blackwell.

992

993

994

2. Rutter,G.A., Pullen,T.J., Hodson,D.J., & Martinez-Sanchez,A. Pancreatic beta cell identity, glucose sensing and the control of insulin secretion. *Biochem. J.* **466**, 202-218 (2015).

995

996

3. Tarasov,A.I. *et al.* The mitochondrial Ca^{2+} uniporter MCU is essential for glucose-induced ATP increases in pancreatic β -cells. *PLoS One* **7**, e39722 (2012).

997

998

4. Xin,Y. *et al.* RNA Sequencing of Single Human Islet Cells Reveals Type 2 Diabetes Genes. *Cell Metab.* **24**, 608-615 (2016).

999

1000

5. Segerstolpe,A. *et al.* Single-Cell Transcriptome Profiling of Human Pancreatic Islets in Health and Type 2 Diabetes. *Cell Metab.* **24**, 593-607 (2016).

1001

1002

6. Li,J. *et al.* Single-cell transcriptomes reveal characteristic features of human pancreatic islet cell types. *EMBO Rep.* **17**, 178-187 (2016).

1003

1004

7. Wang,Y.J. *et al.* Single-Cell Transcriptomics of the Human Endocrine Pancreas. *Diabetes.* **65**, 3028-3038 (2016).

1005

1006

1007

8. Kiekens,R. *et al.* Differences in glucose recognition by individual rat pancreatic B cells are associated with intercellular differences in glucose-induced biosynthetic activity. *J. Clin. Invest.* **89**, 117-125 (1992).

1008

1009

1010

9. Ammala,C. *et al.* Inositol trisphosphate-dependent periodic activation of a Ca^{2+} -activated K^{+} conductance in glucose-stimulated pancreatic β -cells. *Nature* **353**, 849-852 (1991).

1011

1012

1013

10. Benninger,R.K. & Piston,D.W. Cellular communication and heterogeneity in pancreatic islet insulin secretion dynamics. *Trends Endocrinol. Metab.* **25**, 399-406 (2014).

1014

1015

11. Meda,P. *et al.* The topography of electrical synchrony among beta-cells in the mouse islet of Langerhans. *Q. J. Exp. Physiol.* **69**, 719-735 (1984).

1016

1017

1018

12. Palti,Y., David,G.B., Lachov,E., Mida,Y.H., & Schatzberger,R. Islets of Langerhans generate wavelike electric activity modulated by glucose concentration. *Diabetes.* **45**, 595-601 (1996).

1019

1020

1021

13. Benninger,R.K., Zhang,M., Head,W.S., Satin,L.S., & Piston,D.W. Gap junction coupling and calcium waves in the pancreatic islet. *Biophys. J.* **95**, 5048-5061 (2008).

1022

1023

1024

14. Head,W.S. *et al.* Connexin-36 gap junctions regulate in vivo first- and second-phase insulin secretion dynamics and glucose tolerance in the conscious mouse. *Diabetes.* **61**, 1700-1707 (2012).

- 1025 15. Meda,P., Kohen,E., Kohen,C., Rabinovitch,A., & Orci,L. Direct
1026 communication of homologous and heterologous endocrine islet cells in culture.
1027 *J. Cell Biol.* **92**, 221-226 (1982).
- 1028 16. Meda,P., Santos,R.M., & Atwater,I. Direct identification of
1029 electrophysiologically monitored cells within intact mouse islets of Langerhans.
1030 *Diabetes* **35**, 232-236 (1986).
- 1031 17. Rutter,G.A. & Hodson,D.J. Beta cell connectivity in pancreatic islets: a type 2
1032 diabetes target? *Cell Mol. Life Sci.* **72**, 453-467 (2015).
- 1033 18. Hodson,D.J. *et al.* Lipotoxicity disrupts incretin-regulated human beta cell
1034 connectivity. *J. Clin. Invest.* **123**, 4182-4194 (2013).
- 1035 19. Stozer,A. *et al.* Functional connectivity in islets of Langerhans from mouse
1036 pancreas tissue slices. *PLoS Comput. Biol.* **9**, e1002923 (2013).
- 1037 20. Hodson,D.J. *et al.* Existence of long-lasting experience-dependent plasticity in
1038 endocrine cell networks. *Nat. Commun.* **3**, 605 (2012).
- 1039 21. Johnston,N.R. *et al.* Beta cell hubs dictate pancreatic islet responses to
1040 glucose. *Cell Metabolism* **24**, 389-401 (2016).
- 1041 22. Speier,S. *et al.* Noninvasive in vivo imaging of pancreatic islet cell biology.
1042 *Nat. Med.* **14**, 574-578 (2008).
- 1043 23. Tian,L. *et al.* Imaging neural activity in worms, flies and mice with improved
1044 GCaMP calcium indicators. *Nat. Methods.* **6**, 875-881 (2009).
- 1045 24. van der Meulen,T. *et al.* Virgin Beta Cells Persist throughout Life at a
1046 Neogenic Niche within Pancreatic Islets. *Cell Metab.* **25**, 911-926 (2017).
- 1047 25. Chen,C. *et al.* Alterations in beta-Cell Calcium Dynamics and Efficacy
1048 Outweigh Islet Mass Adaptation in Compensation of Insulin Resistance and
1049 Prediabetes Onset. *Diabetes.* **65**, 2676-2685 (2016).
- 1050 26. Singh,S.P. *et al.* Different developmental histories of beta-cells generate
1051 functional and proliferative heterogeneity during islet growth. *Nat. Commun.* **8**,
1052 664-00461 (2017).
- 1053 27. Kimmel,R.A. & Meyer,D. Zebrafish pancreas as a model for development and
1054 disease. *Methods Cell Biol.* **134**, 431-461 (2016).
- 1055 28. Steiner,D.J., Kim,A., Miller,K., & Hara,M. Pancreatic islet plasticity:
1056 interspecies comparison of islet architecture and composition. *Islets.* **2**, 135-145
1057 (2010).
- 1058 29. Bosco,D. *et al.* Unique arrangement of alpha- and beta-cells in human islets
1059 of Langerhans. *Diabetes.* **59**, 1202-1210 (2010).
- 1060 30. Prince,V.E., Anderson,R.M., & Dalgin,G. Zebrafish Pancreas Development
1061 and Regeneration: Fishing for Diabetes Therapies. *Curr. Top. Dev. Biol.* **124**:
1062 235-276 (2017).

- 1063 31. Ninov,N. *et al.* Metabolic regulation of cellular plasticity in the pancreas. *Curr.*
1064 *Biol.* **23**, 1242-1250 (2013).
- 1065 32. Granger,C.W.J. Investigating Causal Relations by Econometric Models and
1066 Cross-spectral Methods. *Econometrica* **37**, 424-438 (1969).
- 1067 33. Barnett,L. & Seth,A.K. The MVGC multivariate Granger causality toolbox: a
1068 new approach to Granger-causal inference. *J. Neurosci. Methods.* **223**, 50-68
1069 (2014).
- 1070 34. Hesselson,D., Anderson,R.M., Beinat,M., & Stainier,D.Y. Distinct populations
1071 of quiescent and proliferative pancreatic beta-cells identified by H0Tcre mediated
1072 labeling. *Proc. Natl. Acad. Sci. U. S. A.* **106**, 14896-14901 (2009).
- 1073 35. Janjuha,S., Pal,S.S., & Ninov,N. Analysis of Beta-cell Function Using Single-
1074 cell Resolution Calcium Imaging in Zebrafish Islets. *J. Vis. Exp.*10 (2018).
- 1075 36. Schindelin,J. *et al.* Fiji: an open-source platform for biological-image analysis.
1076 *Nat. Methods.* **9**, 676-682 (2012).
- 1077 37. Ollion,J., Cochenec,J., Loll,F., Escude,C., & Boudier,T. TANGO: a generic
1078 tool for high-throughput 3D image analysis for studying nuclear organization.
1079 *Bioinformatics.* **29**, 1840-1841 (2013).
- 1080 38. Preibisch,S., Saalfeld,S., Schindelin,J., & Tomancak,P. Software for bead-
1081 based registration of selective plane illumination microscopy data. *Nat. Methods.*
1082 **7**, 418-419 (2010).
- 1083 39. Kone,M. *et al.* LKB1 and AMPK differentially regulate pancreatic beta-cell
1084 identity. *FASEB J.* **28**, 4972-4985 (2014).
- 1085 40. Thorens,B. *et al.* Ins1 knock-in mice for beta cell-specific gene recombination.
1086 *Diabetologia* **58**, 558-656 (2015).
- 1087 41. Luo,J. *et al.* A protocol for rapid generation of recombinant adenoviruses
1088 using the AdEasy system. *Nat. Protoc.* **2**, 1236-1247 (2007).
- 1089 42. Ravier,M.A. & Rutter,G.A. Isolation and culture of mouse pancreatic islets for
1090 *ex vivo* imaging studies with trappable or recombinant fluorescent probes.
1091 *Methods Mol. Biol.* **633**, 171-184 (2010).
- 1092 43. Janjuha,S. *et al.* Age-related islet inflammation marks the proliferative decline
1093 of pancreatic beta-cells in zebrafish. *Elife.* **7.**, 32965 (2018).
- 1094 44. Zheng,G.X. *et al.* Massively parallel digital transcriptional profiling of single
1095 cells. *Nat. Commun.* **8**:14049 (2017).
- 1096 45. Baron,M. *et al.* A Single-Cell Transcriptomic Map of the Human and Mouse
1097 Pancreas Reveals Inter- and Intra-cell Population Structure. *Cell Syst.* **3**, 346-360
1098 (2016).
- 1099 46. Butler,A., Hoffman,P., Smibert,P., Papalexi,E., & Satija,R. Integrating single-
1100 cell transcriptomic data across different conditions, technologies, and species.
1101 *Nat. Biotechnol.* **36**, 411-420 (2018).

- 1102 47. Mi,H. *et al.* PANTHER version 11: expanded annotation data from Gene
1103 Ontology and Reactome pathways, and data analysis tool enhancements.
1104 *Nucleic Acids Res.* **45**, D183-D189 (2017).
- 1105 48. Gut,P. *et al.* Whole-organism screening for gluconeogenesis identifies
1106 activators of fasting metabolism. *Nat. Chem. Biol.* **9**, 97-104 (2013).
- 1107 49. Markovic,R. *et al.* Progressive glucose stimulation of islet beta cells reveals a
1108 transition from segregated to integrated modular functional connectivity patterns.
1109 *Sci. Rep.* **5**, 7845 (2015).
- 1110 50. Diraison,F. *et al.* Over-expression of sterol-regulatory-element-binding
1111 protein-1c (SREBP1c) in rat pancreatic islets induces lipogenesis and decreases
1112 glucose-stimulated insulin release: modulation by 5-aminoimidazole-4-
1113 carboxamide ribonucleoside (AICAR). *Biochem. J.* **378**, 769-778 (2004).
- 1114 51. Rodriguez-Diaz,R. *et al.* Noninvasive in vivo model demonstrating the effects
1115 of autonomic innervation on pancreatic islet function. *Proc. Natl. Acad. Sci. U. S.*
1116 *A.* **109**, 21456-21461 (2012).
- 1117 52. Ilegems,E. *et al.* Light scattering as an intrinsic indicator for pancreatic islet
1118 cell mass and secretion. *Sci. Rep.* **5**, 10740 (2015).
- 1119 53. Nyqvist,D. *et al.* Donor islet endothelial cells in pancreatic islet
1120 revascularization. *Diabetes.* **60**, 2571-2577 (2011).
- 1121 54. Westacott,M.J., Ludin,N.W.F., & Benninger,R.K.P. Spatially Organized beta-
1122 Cell Subpopulations Control Electrical Dynamics across Islets of Langerhans.
1123 *Biophys. J.* **113**, 1093-1108 (2017).
- 1124 55. Reinbothe,T.M., Safi,F., Axelsson,A.S., Mollet,I.G., & Rosengren,A.H.
1125 Optogenetic control of insulin secretion in intact pancreatic islets with beta-cell-
1126 specific expression of Channelrhodopsin-2. *Islets.* **6**, e28095 (2014).
- 1127 56. Lorincz,R. *et al.* In vivo monitoring of intracellular Ca(2+) dynamics in the
1128 pancreatic beta-cells of zebrafish embryos. *Islets.* **10**, 221-238 (2018).
- 1129 57. Gosak,M. *et al.* Critical and Supercritical Spatiotemporal Calcium Dynamics in
1130 Beta Cells. *Front Physiol.* **8**, 1106 (2017).
- 1131 58. Ammala,C., Ashcroft,F.M., & Rorsman,P. Calcium-independent potentiation
1132 of insulin release by cyclic AMP in single beta-cells. *Nature.* **363**, 356-358 (1993).
- 1133 59. Lu,T.T. *et al.* The Polycomb-Dependent Epigenome Controls beta Cell
1134 Dysfunction, Dedifferentiation, and Diabetes. *Cell Metab.* **27**, 1294-1308 (2018).
1135
1136
1137
1138

1139 **Figure legends**

1140 **Figure 1. Glucose-stimulated Ca^{2+} influx imaged *in vivo* in the living zebrafish.**

1141 **a.** Cartoon representing a transgenic zebrafish larva expressing the genetically-encoded
1142 Ca^{2+} indicator GCaMP6s (green) and the nuclear marker cdt1-mCherry (red) under the
1143 insulin promoter. GCaMP6s allows the examination of glucose-induced Ca^{2+} -influx in the β
1144 cell reported by changes in the green fluorescence in a Ca^{2+} concentration-dependent
1145 fashion. **b.** Maximum intensity projections of an islet imaged before, during and after the
1146 intra-cardiac injection of 5 nL of 25 mM glucose solution. Imaging and glucose stimulation
1147 were performed simultaneously. Note the near-synchronous increase in GCaMP6
1148 fluorescence intensity across all the β cells in the islet upon glucose injection. **c.** A trace
1149 showing cumulative normalized fluorescent intensity over time for the cells shown in A. The
1150 black arrow marks the instance of the glucose injection. **c'.** Normalized fluorescence
1151 intensity over time for each individual cell. Each cell is represented by a square. The
1152 normalized GCaMP6 fluorescence is displayed as a heat-map, showing the degree of cell
1153 activity ($n=10$ animals, not graphically represented here). **d.** Quantification of the islet
1154 response to glucose stimulation. The graph depicts the GCaMP6 area under the curve
1155 covering 100 seconds before and 100 seconds after the glucose stimulation ($n=3$, paired two
1156 tail t-test, $P=0.0108$, data are means \pm SD). The injection of glucose led to a dramatic
1157 increase in GCaMP6 fluorescence intensity. **e.** Changes in measured free glucose
1158 concentration in larvae following glucose injection as in A. Each dot represents a pool of 10
1159 injected larvae. ($n=3$ for each time point, one-tailed ANOVA, with Tukey's multiple
1160 comparisons test, $P=0.0488$ for 0 vs. 5min and $P=0.0152$ for 5 vs. 15min). Data are means
1161 \pm SD. Scale bars, 10 μm . The cartoons shown in panel (a) belong to the authors of this
1162 study. The experiments in **b,c** were performed three independent times with several samples
1163 showing similar results. **d** shows a quantification from three biological replicates from one of
1164 the repeats. The experiment in **e** was performed once with multiple samples.

1165

1166

1167 **Figure 2. Ca^{2+} dynamics and connectivity in zebrafish: slow imaging acquisition (frame**
1168 **rate 0.1Hz).**

1169 **a.** Single confocal planes acquired during each time window (labelled i-v) show an increase
1170 in GCaMP fluorescence intensity during time window iii (i.e. coinciding with intracardiac
1171 glucose injection) but no strong GCaMP signal before glucose injection (time windows i-ii)
1172 or after glucose injection (time windows iv-v). Time windows i-v were 100 s long. **b.**
1173 Representation of a normalised fluorescence trace generated by each β -cell region of

1174 interest (ROI) across the entire imaging session (1,200 s). Time windows (100s) labelled i-v
1175 are shown at the top and the dashed line represents the time of intra-cardiac glucose
1176 injection. T_{20} was defined as the time taken between glucose injection and the calcium
1177 intensity spike to reach 20% above baseline. This value is tabulated for each ROI, thereby
1178 identifying cell 2 and cell 6 as “leaders”. **c.** Cartesian functional connectivity maps displaying
1179 the x-y position of analysed cells (numbered black dots). Cells are connected with a
1180 coloured line if the p statistic for the Pearson coefficient was < 0.001 post bootstrapping.
1181 The strength of the cell pair correlation (the Pearson R statistic) was colour coded: red for R
1182 of 0.75 to 1.0, yellow for R of 0.5 to 0.75 and green for R of 0.25-0.5. Results confirm an
1183 increase in cell-cell connectivity (strength AND number) during glucose injection (time
1184 window iii). **d.** Heat maps show the Pearson coefficient of each cell pair in a colour-coded
1185 manner (negative correlation; dark brown (-1), no correlation; mid brown (0), high correlation;
1186 yellow/white (1)). **e.** During time window iii (ie at time of glucose injection) the mean positive
1187 Pearson coefficient for connected cell pairs is 0.75 +/- 4.08 (SEM), significantly higher than
1188 before or after glucose injection (window i R 43.8 +/-1.46, ii R 0.48 +/- 2.59, iv R 46.4 +/- 5.3
1189 and v R 0.35 +/- 3.45) (P<0.001 on one way ANOVA with Tukey’s multiple comparison). **f.**
1190 The overall percentage of connected cell pairs is elevated (46% +/- 6.18% SEM) during the
1191 glucose injection compared to the rest time points (window i 15.3% +/- 2.4, window ii 10% +/-
1192 1.86, iv 18.6% +/- 4.6 and window v 11.1% +/- 2.7). (n=6, P<0.001 one way ANOVA with
1193 Tukey’s).

1194
1195

1196 **Figure 3. Ca^{2+} dynamics and connectivity examined in zebrafish during rapid image**
1197 **acquisition.**

1198 **a.** Example islet single confocal slices acquired at 3 frames/s before and during glucose
1199 injection. Associated Cartesian connectivity maps and Pearson heatmaps (as described in
1200 detail in Figure 2) are given below. **b.** Ca^{2+} traces from individual ROIs in the imaged islet.
1201 The dashed line represents the time of intracardiac glucose injection. As described in Figure
1202 2, the time to 20% rise in Ca^{2+} signal post glucose injection was measured, and tabulated in
1203 order to identify the first responders or “temporal leaders”. **c.** Pooled data for the five
1204 animals imaged. The mean Pearson coefficient of correlation rose significantly from the low
1205 to high glucose state (n=5, data are means \pm SEM, p<0.001 on paired two-tailed t-test). **d.**
1206 The percentage of significantly connected cell pairs also increases significantly following
1207 glucose administration. Data are means \pm SEM and **p<0.01 following a paired two-tailed t-
1208 test). **e.** 3D islet projections acquired at 0.8 Hz before and during glucose injection. **f.**
1209 Associated 3D map showing the time of response in a colour-key fashion (red colour

1210 represents the fastest response). **g.** Cartesian connectivity map and Pearson heatmaps for
1211 the islet shown in e ($n=3$ animals, not graphically represented here). The experiment in **e,f,g**
1212 was performed once with three samples showing similar results.

1213

1214

1215 **Figure 4. Ablation of temporally-defined “leader” cells (but not follower cells) alters**
1216 **islet responsivity to glucose *in vivo* in the zebrafish.**

1217 **a-b.** Images from the time-lapse recording (six frames/second, single plane) of the islet
1218 following three consecutive glucose stimulations before and after “leader” or “follower”
1219 (control) cell ablation. Glucose was injected at 5 min. intervals whilst Ca^{2+} dynamics were
1220 monitored. After the identification of presumptive “follower” or “leader” cells, these cells were
1221 ablated using a two-photon laser ablation (see Methods). An X. indicates the targeted cells.
1222 The top panels show representative frames from the movies before and after the ablation of
1223 a “follower” (a) or a “leader” cell (b). The lower traces (a'-b') show the normalized GCaMP6
1224 fluorescence traces and the peak in Ca^{2+} influx following glucose injection pre- and post-
1225 ablation. **c.** Quantification of the Area Under the Curve (A.U.C.) reflecting 200 frames of
1226 normalized GCaMP6 fluorescence before and after the ablation of a “follower” or a “leader”
1227 cell ($n = 20$ islets each) (paired two-tailed t-test, $P= 3.43 \times 10^{-5}$, ns: not significant). The
1228 ablation of “leader”, but not “follower” cells, led to a significant reduction in the total islet
1229 GCaMP response. Each data-point represents the mean A.U.C from three glucose-
1230 injections in individual larvae. Data are means \pm SD. The experiments were performed eight
1231 independent times with several samples showing similar results.

1232

1233 **Figure 5. Ca^{2+} waves and connectivity revealed using islets expressing GCaMP6f**
1234 **throughout the cell population under insulin promoter control.**

1235 **a.** (i) Image of a donor islet that implanted onto the iris of a syngeneic recipient. Islets
1236 indicated with arrows. (ii) Individual cells identified within a single islet were analysed. **b.**
1237 Imaging for 10 minutes at 1fps of an islet that was exposed to chronically elevated circulating
1238 glucose levels (measured values indicated at the time points they were measured along the
1239 top). Ca^{2+} traces from 50 individual β cell ROIs are superimposed, demonstrating retained
1240 coordination of wave behaviour over time **c.** Pearson heat maps and Cartesian connectivity
1241 maps in two dimensions (2D – upper four panels) and 3D (lower four panels). The sharp
1242 increase in β cell connectivity occurs in 3D across the entire islet and mirrors what is
1243 captured in 2D (single plane). **d** and **e.** Pooled data for the three animals imaged in 3D.
1244 Note that the rise in mean Pearson coefficient of β cell connectivity and proportion (%) of
1245 cells connected in the low *versus* high glucose state in 3D was comparable to that measured

1246 in 2D. 2D image dataset ($n=5$ islets in 5 different animals, not graphically represented here)
1247 revealed a mean rise in Pearson R from 46.4 ± 7.2 to 92.6 ± 0.9 ($P < 0.01$ on two-tailed t-
1248 test) and rise in % connectivity from $19.7 \pm 5.5\%$ to $88.8 \pm 5.9\%$ ($P < 0.001$ on two-tailed
1249 t-test).

1250

1251

1252 **Figure 6. Binarized and Granger causality analysis corroborates the existence of**
1253 **super-connected leader cells in mouse islets *in vivo*.** **a.** Pooled data for average R and
1254 % connectivity measurements in mouse islets ($n=5$ in 5 different animals, individual
1255 datapoints shown) imaged over 60 minutes, with prolonged (>10 minute) exposure to high
1256 circulating glucose levels. Connectivity was recorded in the high glucose state (>10 mM),
1257 medium (6-10mM) and low (<4 mM) state from the same β cell ROIs. Prolonged exposure
1258 to high glucose levels does not abrogate the connectivity readout or result in dysynchrony. **b.**
1259 Topographic representation of connected β cells as extracted using the binarized and Monte
1260 Carlo data analysis approach for the same islet shown in Figure 5. Topographical
1261 representation of β cell connections in the remaining four islets imaged are shown in **b'**. The
1262 top 20-40% connected cells (reminiscent of previously-defined *in vitro* hubs) are highlighted
1263 in white. **c.** Log-log graph of the distribution of cell-cell connections pooled across all five
1264 islets imaged reveals a scale-free network (obeying a power-law distribution) whereby 8%
1265 cells serve the majority (60-100%) connections. **d.** Section of fluorescence intensity
1266 readouts for all 26 cells identified during a typical Ca^{2+} wave (superimposed in different
1267 colours) in a single islet. Data collected at 1.0 frame per second, the calcium waves shown
1268 here occurred in the high glucose state (25 mM). **e.** Close up of the fluorescent profiles for
1269 each individual cell taking part in the islet Ca^{2+} wave. "Leader cells" can be defined
1270 temporally as preceding the activity of "follower" cells. **f.** Yellow markers highlight the
1271 position of the temporally-defined "leaders". Results are shown in Supplementary Table 1
1272 (Animal #1). Note that temporally the four defined "leaders" are always the most connected
1273 on independent Granger Causality analysis.

1274

1275

1276

1277

1278

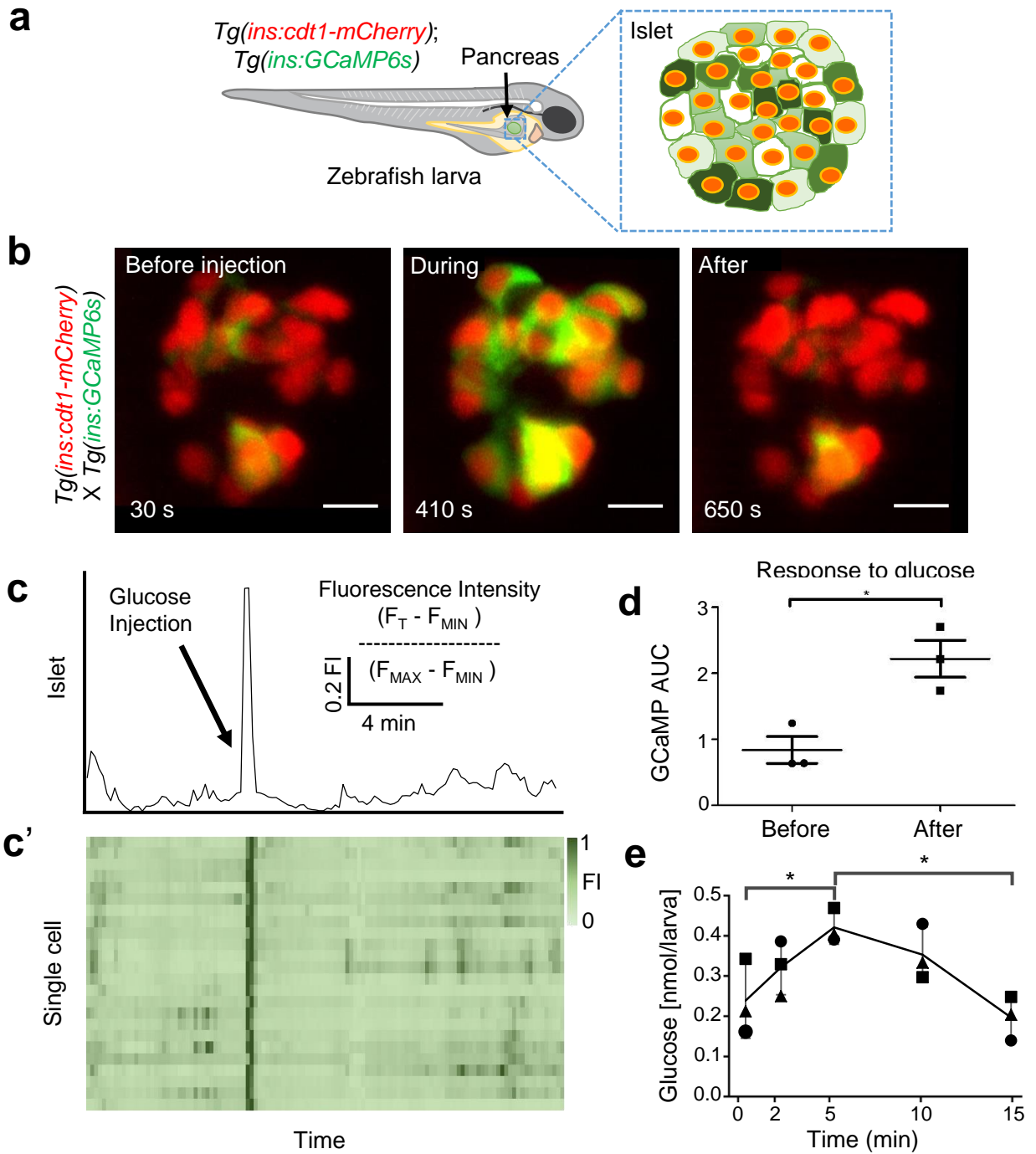


Figure 1

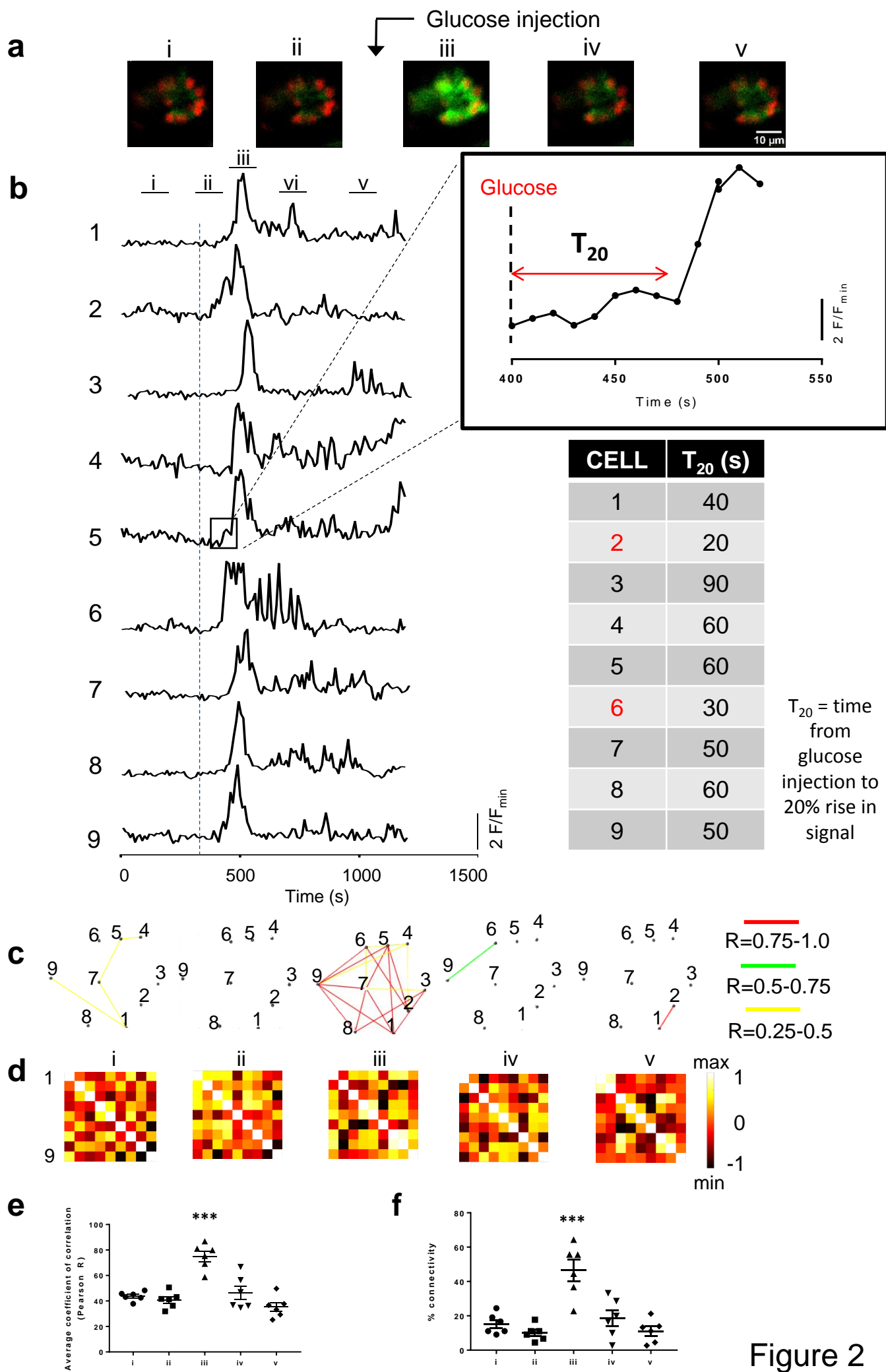


Figure 2

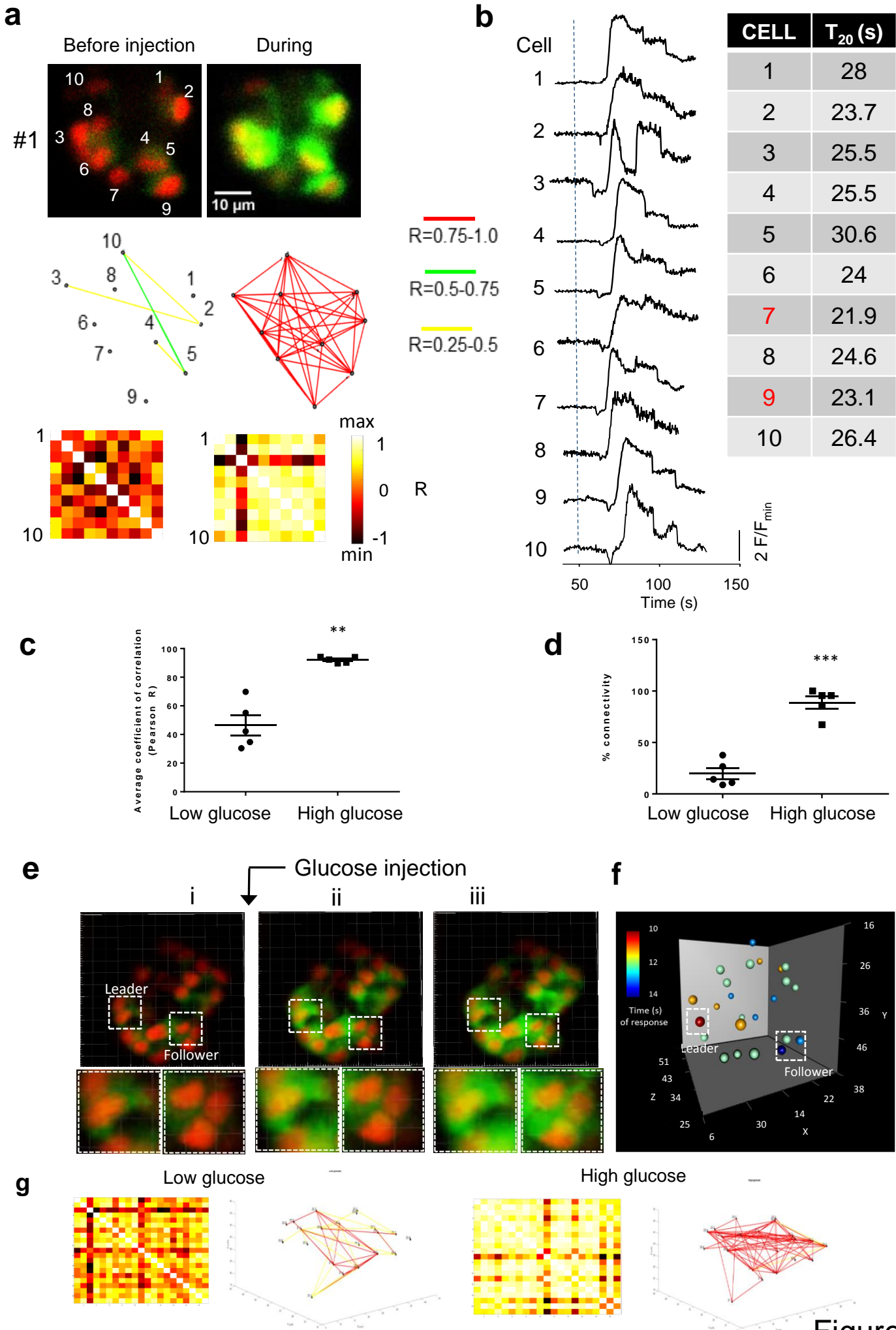


Figure 3

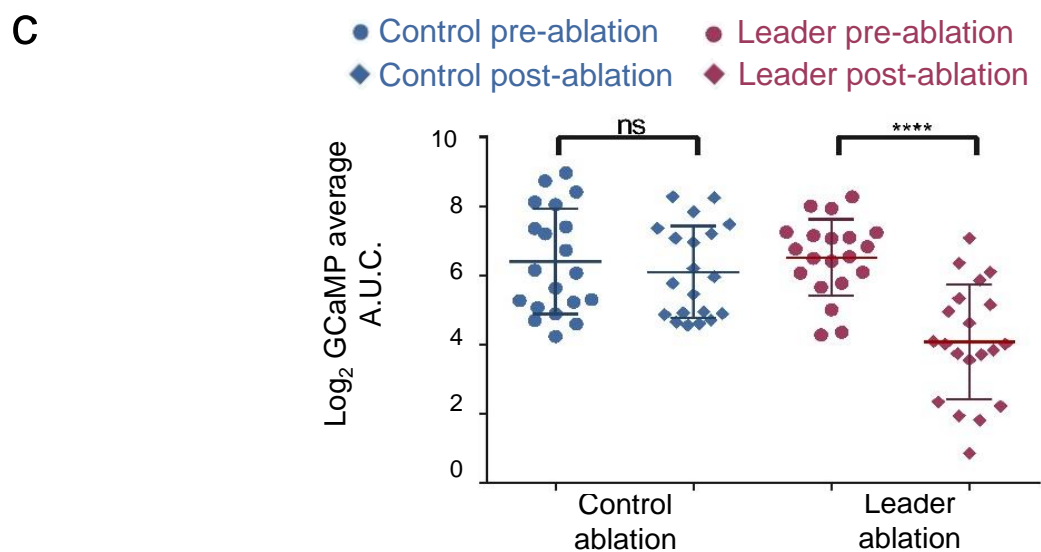
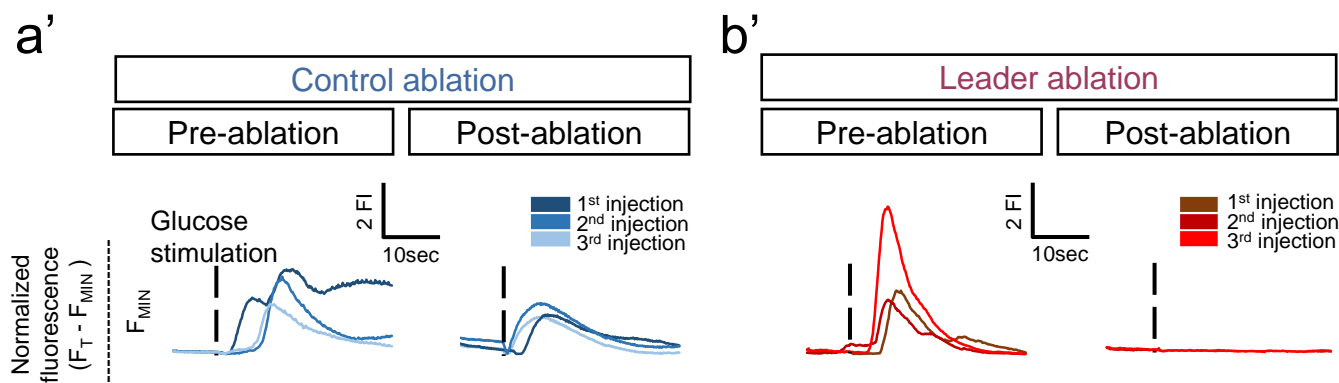
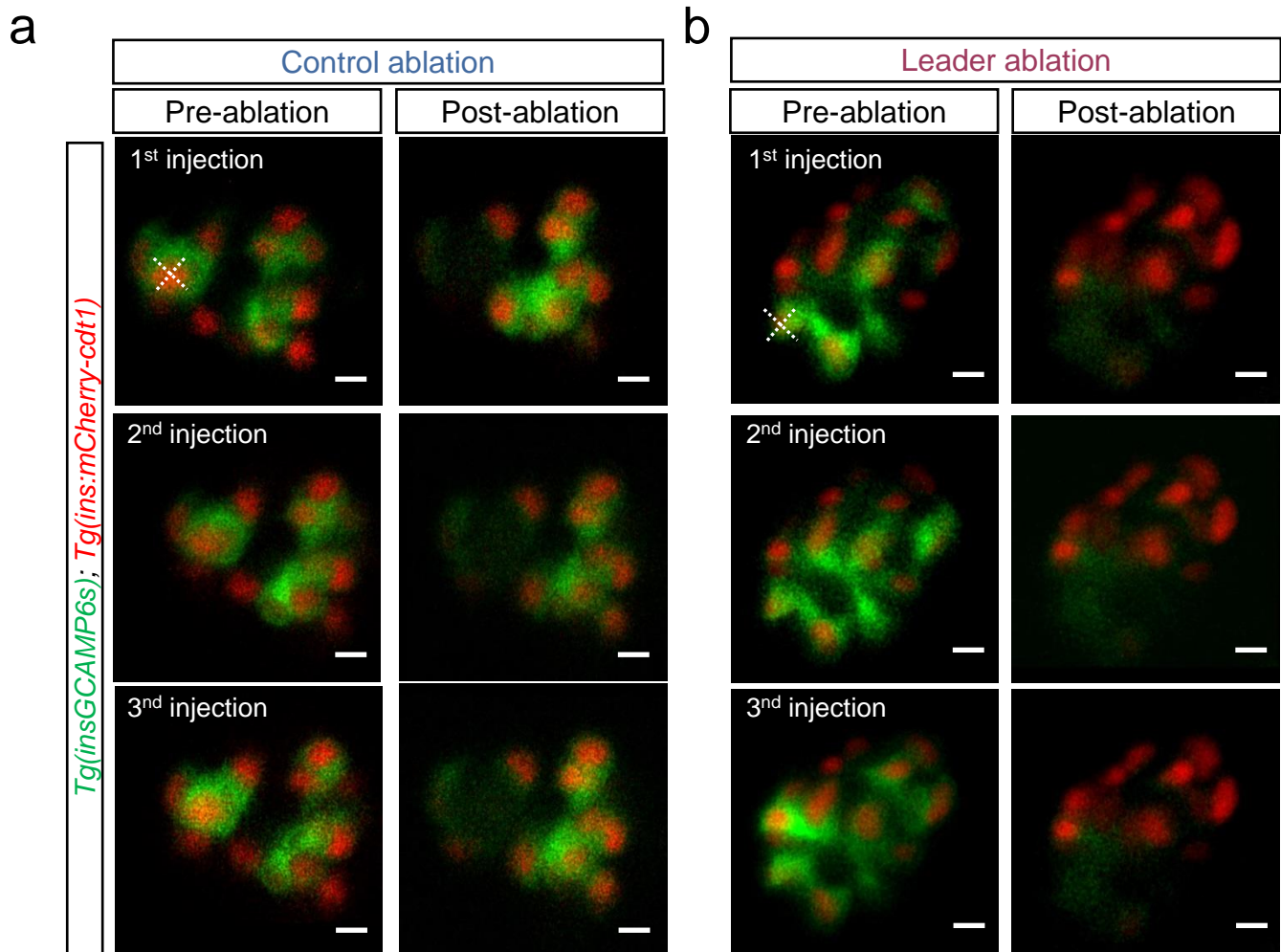


Figure 4

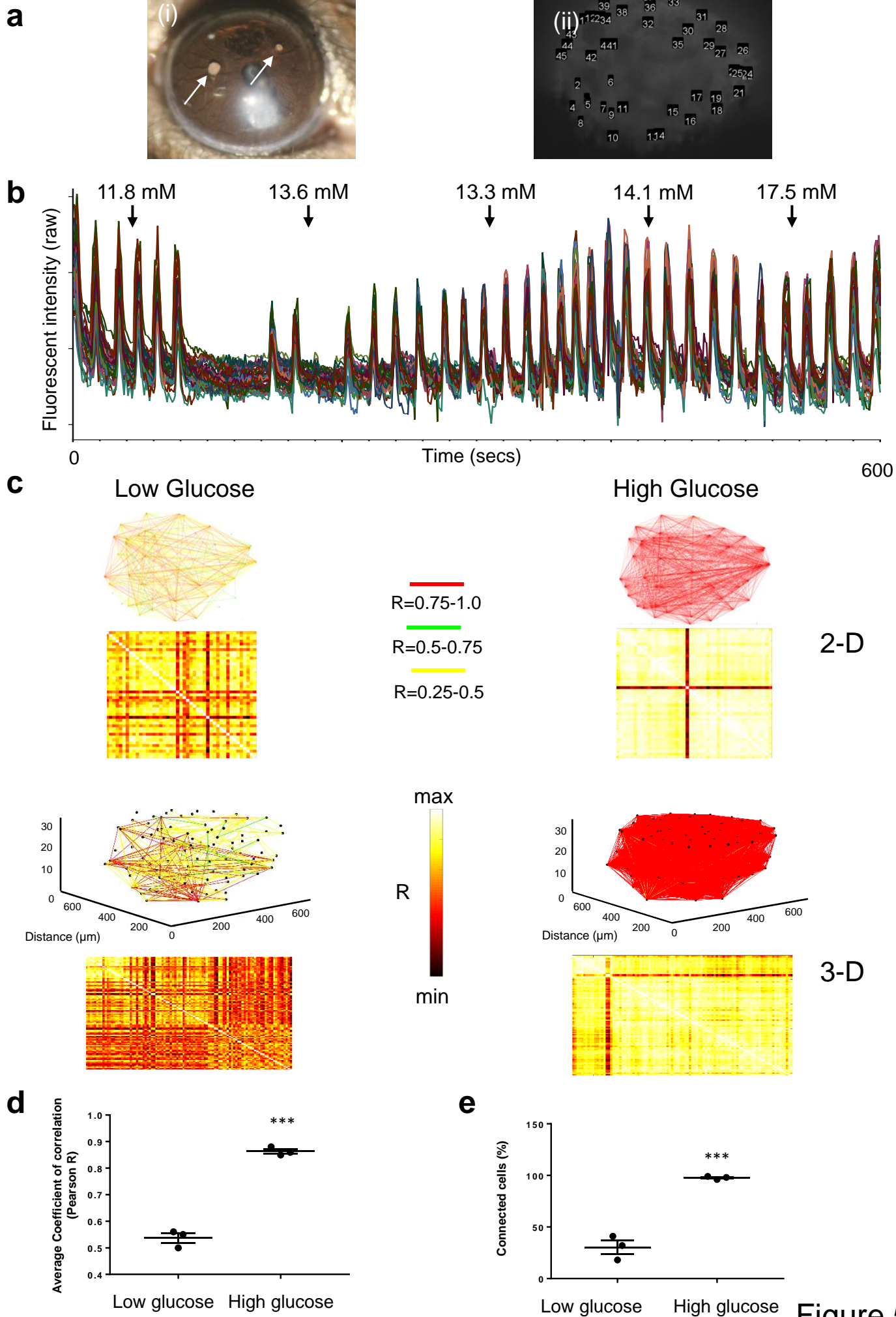


Figure 5

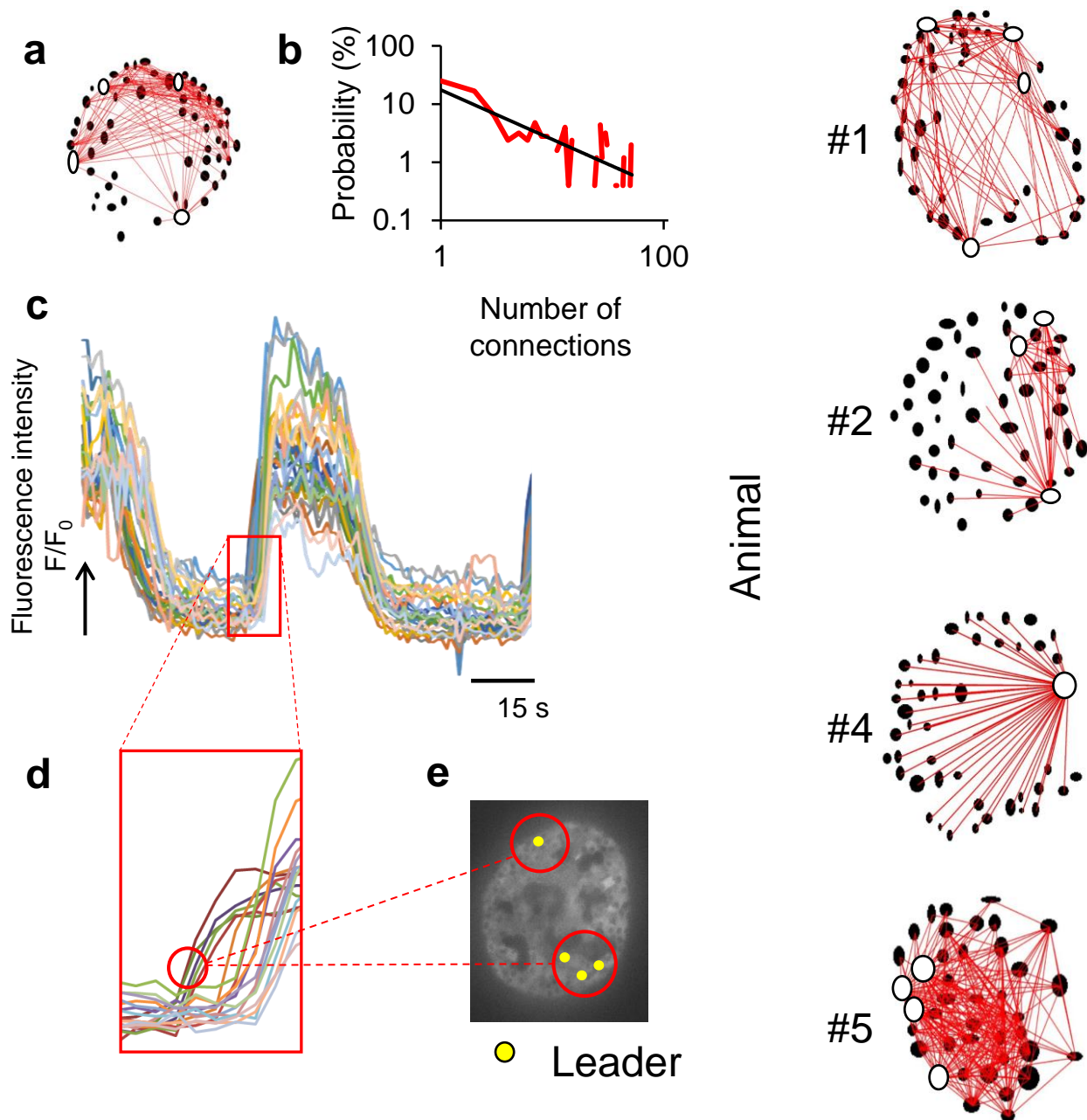
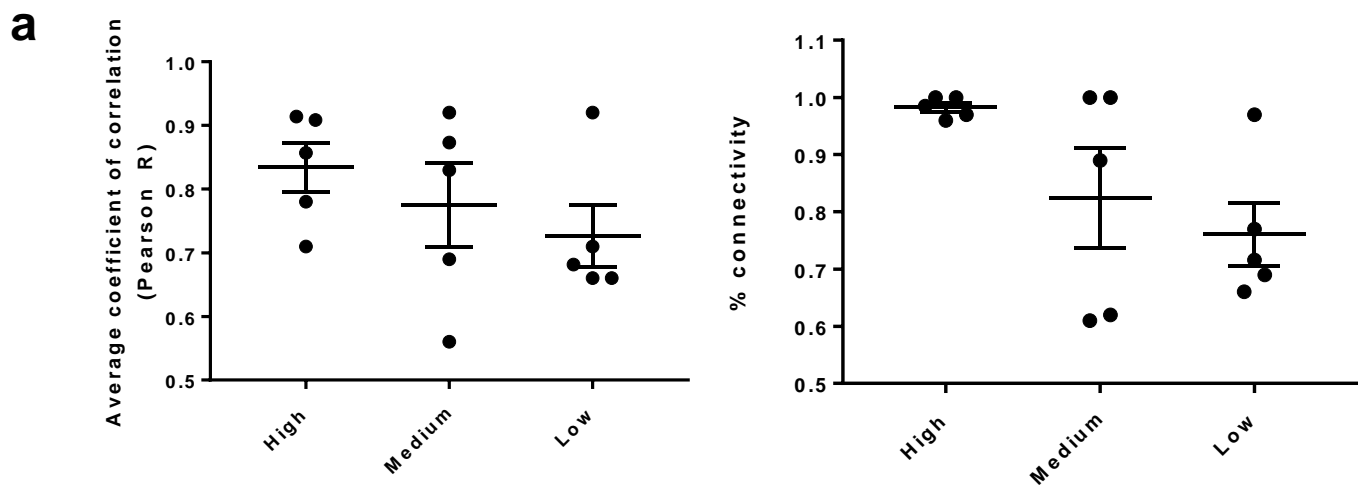


Figure 6